Optically Detected Electrochemistry on Semiconductor Nanocrystals

Master Thesis

Master Thesis

Optically Detected Electrochemistry on Semiconductor Nanocrystals

David Plotzki

Born   July 10, 1986 in Leipzig

Department   Abteilung Molekulare Nanophotonik,
Institut für Experimentelle Physik I,
Fakultät für Physik und Geowissenschaften,
Universität Leipzig

Leipzig, November 03, 2014

Contents

1 Introduction

Semiconductor nanocrystals are artificial nanoscale particles. They usually consist of about 10 000 atoms and are either epitaxially grown on substrates, [1] or—as for the crystals studied in this work—synthesized freely floating in solution, [2] which results in crystals of spherical shape, called colloidal nanocrystals. Often, they are referred to as *quantum dots* because the spacial extent of their semiconductor lattices is strongly shortened in all three dimensions. For this reason they are sometimes treated as zero-dimensional objects. The small size heavily confines the wave function of free charge carriers in all directions and therefore leads to strongly localized quantum states. Thereby, they gain electric and optical properties intermediate between three-dimensional bulk semiconductors on the one side and molecules and atoms on the other. For example, the strong quantum confinement leads to discrete energy states—similar to atoms—in the conduction and valence band, which are considered continuous for bulk semiconductors. However, the density of states is still higher than for single atoms or molecules.

Quantum dots have first been studied in the early 1980s [3] and drawn an increasing research interest ever since. It was clear from the beginning that their unique properties could be employed in numerous applications. First of all, their final size can be very precisely controlled during the growth process. This means that the optical band gap and therefore the fluorescence emission wavelength are finely tunable through the strength of the quantum confinement. Today it is possible to grow highly monodisperse nanocrystal ensembles. [2] This makes them suitable for utilization in quantum dot lasers [4, 5] and light-emitting devices (LEDs). [6, 7] They are further used in solar cells [8, 9] and as biological markers, in vivo fluorophores and cellular probes. [10, 11] Quantum dots can also be employed as single photon emitters, which might allow applications in quantum computing and quantum cryptography. [12, 13]

These applications often encounter challenges that arise from another interesting optical property of the nanocrystals. Their fluorescence signal randomly switches between »on« and »off« states, and intermediate states are known as well. [14, 15, 16] This fluorescence intermittency, called »blinking«, is also found in molecular fluorophores. Its origin is not yet fully understood and still subject of discussion. Usually associated with charges, especially electron or hole injection and ejection, [17, 18] and the interplay with the dielectric environment, [19] it is of crucial importance to understand the underlying processes in order to develop optimization strategies for the aforementioned applications.

In the language of chemistry, the selective reduction or oxidation of the quantum dots should lead to visible changes in their fluorescence behavior. The approach taken in this work is to combine electrochemical methods with time-tagged, time-resolved fluores-

cence microscopy to study the influence of charging or discharging at specific electric potentials on the nanocrystal luminescence and excited state lifetime. The quantum dot sample is adsorbed to a transparent semiconductor electrode, which allows both excitation and fluorescence detection at wavelengths in the optical spectrum.

The quantum dots studied here exhibit a CdSe core of about 4 nm in diameter (fig. 1.1). To saturate surface defects and protect them from oxidation, a ZnS shell of about two atomic monolayers has been grown around the core. For further passivation, hexadecy-lamine (HDA) ligands are added to coordinate with unsaturated surface sites (see right picture in fig. 1.1). The quantum dots are bought from Evident Technologies. They come solved in toluene with excess HDA ligands in the solution, and are spin coated onto the flat semiconductor electrodes. For details, see chapter 3.
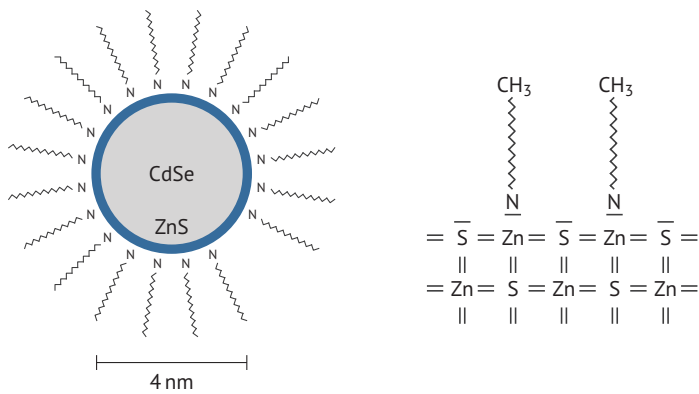
Fig. 1.1: (Left) CdSe/ZnS core/shell quantum dot of the typical size used in this work, with hexadecy-lamine (HDA) ligands attached to the outer shell. The surface coverage with ligands is not assumed to be complete. **(Right)** Illustration of the surface structure. The lone electron pairs of the ligands' nitrogen atoms coordinate with unsaturated Zn surface sites.

2 Theoretical Background

2.1 Semiconductor Nanocrystals

2.1.1 Lattice Properties and Electronic Band Structure

Semiconductor materials have become an important cornerstone in nanoscale science. They exhibit useful electric and optical properties, many of which can be easily tuned by doping the lattice with impurities or creating alloys of different materials. In the case of spherical core/shell quantum dots, two different semiconductors are joined to create wells that lead to charge carrier confinement.

To understand the properties and optical behavior of quantum dots, it is therefore necessary to consider the nature of semiconductors.

Many semiconductors form crystal lattices of one or two atomic species. The quantum dots investigated in this thesis have cores made of CdSe, a crystalline material that features a **wurtzite structure** (fig. 2.1c) under normal conditions. [20] It is formed by a hexagonal Bravais lattice (fig. 2.1a) with a basis that consists of two atoms separated by a distance $d = \sqrt{3/8} \cdot a$ in units of the hcp lattice constant a (fig. 2.1b). This leads to a tetrahedral arrangement: each atom is bound to four partner atoms at a distance d (fig. 2.1c). These bonds form the typical tetrahedron angles of 109.47°. d is therefore the universal bond length within the crystal.

The quantum dot shells consist of ZnS, here also in the form of a wurtzite structure. The lattice parameters for both CdSe and ZnS are listed in table 2.1.

In single atoms, the electrons occupy discrete energy levels. The corresponding wave functions are solutions of the Schrödinger equation of an electron that experiences the Coulomb potential of the nucleus, possibly partially shielded by other electrons and influenced by many different factors such as external fields or spin coupling. The probability densities of these wave functions form symmetric orbitals in space which are identified by a set of quantum numbers.

For solids that consist of a multitude of atoms, the wave functions of these orbitals overlap to a high degree. This leads to a rearrangement of the atomic energy levels because

	a [Å]	c [Å]	d [Å]
CdSe	4.299	7.015	2.631
ZnS	3.811	6.234	2.337

Tab. 2.1: Lattice properties [21] of CdSe and ZnS in the wurtzite structure (see fig. 2.1).

(a) hcp lattice   (b) diatomic basis   (c) wurtzite structure
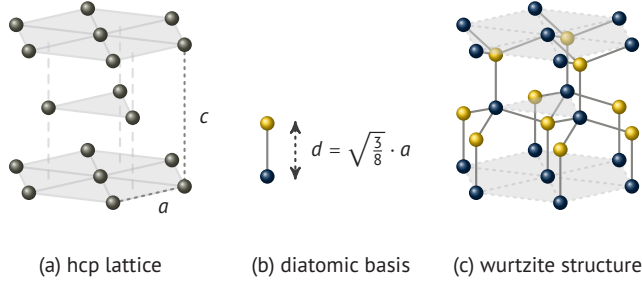
Fig. 2.1: (a) The hexagonal close-packed (hcp) structure with its two lattice constants *a* and *c*. In the ideal case it holds $c/a = \sqrt{8/3}$. All lines are guides for the eye. **(b)** Each site in the hcp lattice is stocked with a diatomic basis to construct the wurtzite structure. The basis atoms are separated by the bond length *d*. **(c)** In the wurtzite structure, each atom has a coordination number of four and arranges in an equidistant, tetrahedral manner to the neighboring atoms. Pictures adopted from Grundmann.[20]

the Pauli principle forbids electrons of the same energy and quantum numbers to occupy the same space. In such a solid, discrete energy levels can no longer be identified. Instead, *energy bands* form, meaning regions of allowed energies. The spaces between these energy bands are called *band gaps* and identify energy regions that are not allowed to be occupied by any electron within the crystal.

To calculate the properties of the energy bands, a periodic electrostatic potential U from the lattice nuclei is assumed:

$$U(\vec{r}) = U(\vec{r} + \vec{R}), \tag{2.1}$$

where the vector $\vec{r}$ represents the coordinates of any point in the lattice and $\vec{R}$ is an arbitrary lattice vector, i.e. a linear combination of the linearly independent base vectors of the Bravais lattice. Assuming an infinite lattice, this means that the lattice properties are invariant under a translation by $\vec{R}$ and consequently, all physical properties exhibit the periodicity of the lattice. Therefore, any electron wave function $\psi(\vec{r})$ that solves the time-independent Schrödinger equation,

$$\left[-\frac{\hbar^2}{2m}\Delta + U(\vec{r}) \right] \psi(\vec{r}) = E\psi(\vec{r}), \tag{2.2}$$

must have a probability density that obeys the lattice periodicity:

$$|\psi(\vec{r})|^2 = |\psi(\vec{r} + \vec{R})|^2. \tag{2.3}$$

This challenge is solved by a *Bloch wave*[22]

$$\psi_{n,\vec{k}}(\vec{r}) = u_{n,\vec{k}}(\vec{r}) \cdot e^{i\vec{k}\cdot\vec{r}}, \tag{2.4}$$

which can be seen as a plane de Broglie wave, modulated by a *Bloch function* $u_{n,\vec{k}}(\vec{r})$

that has the same periodicity as the lattice:

$$u_{n,\vec{k}}(\vec{r}) = u_{n,\vec{k}}(\vec{r} + \vec{R}). \tag{2.5}$$

Each possible solution of the Schrödinger equation (eq. 2.2) is given a distinct quantum number n which corresponds to an energy band. These bands form because there is a continuous family of Bloch functions for all possible wave vectors $\vec{k}$ and therefore also the energy eigenvalues depend on $\vec{k}$.

To calculate the morphology of the energy bands E_n, the **effective mass** m^* of a particle in the band is considered:

$$m^* = \hbar^2 \left[\frac{d^2 E_{n,\vec{k}}}{dk^2} \right]^{-1}. \tag{2.6}$$

Note that the effective mass depends on the wavenumber $k = |\vec{k}|$ and therefore on the direction of the particle wave relative to the lattice. For this reason, the effective mass is actually a tensor.

A simplified approach is the *effective mass approximation* (Norris[23]) that treats the electrons as free particles with a scalar, isotropic effective mass m^* which accounts for the Coulomb potential from the nuclei. To achieve the scalar nature, the second derivative (eq. 2.6) needs to be isotropic, which can be done by a quadratic energy dispersion: $E \sim k^2$.

Norris argues that for semiconductors like CdSe which are of the direct-gap type, i.e. where a transition from the valence to the conduction band requires no momentum change ($\Delta k = 0$), both the maximum of the **valence band (VB)** and the minimum of the **conduction band (CB)** can be placed at $\vec{k} = 0$ (at the Γ point of the first Brillouin zone).

With this prerequisite, eq. 2.6 can be solved in such a way that the resulting energy parabolas (in k-space, fig. 2.2, left) have extrema situated at $k = 0$:

$$E_{\text{VB}} = -\frac{\hbar^2 k^2}{2m_{\text{h}}^*}, \qquad\qquad E_{\text{CB}} = \frac{\hbar^2 k^2}{2m_{\text{e}}^*} + E_{\text{gap}}, \tag{2.7}$$

where m_{h}^* denotes the effective mass of a hole in the valence band and m_{e}^* the effective mass of an electron in the conduction band. Due to energy conservation, the energy dispersion of the holes has the opposite sign of the one for electrons. The size of the energy gap is measured by E_{gap} at $k = 0$. The valence band maximum is placed at $E = 0$ in this convention.

The elements in the CdSe core and in the ZnS shell have the following electron configurations:

Cd: $[\text{Kr}]\, 4d^{10}\, 5s^2$, $\qquad\qquad$ Zn: $[\text{Ar}]\, 3d^{10}\, 4s^2$,

$\ $ Se: $[\text{Ar}]\, 3d^{10}\, 4s^2\, 4p^4$, $\qquad\qquad$ S: $[\text{Ne}]\, 3s^2\, 3p^4$.

Both CdSe and ZnS are type II-VI semiconductors because their valence shells are stacked with two (Cd, Zn) and respectively six (Se, S) electrons. There are the following two scenarios for the compound atoms to form chemical bonds [24] (only CdSe is discussed).

- *Ionic bond scenario:* The cadmium atoms donate their valence s-electrons to the energetically lower p-orbitals of the selenium atoms. Each atom reaches a fully occupied valence shell. This leads to charged ions (Cd^{2+}, Se^{2-}) that are bound by their Coulomb potentials.

$$Cd(5s^2) + Se(4s^2 4p^4) \longrightarrow Cd^{2+}(5s^0) + Se^{2-}(4s^2 4p^6)$$
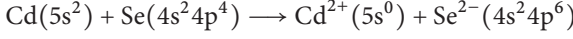
- *Covalent bond scenario:* An LCAO approach (linear combination of atomic orbitals) is used where both kinds of atoms in the compound develop sp^3 hybrid orbitals. This leads to a number of four tetrahedrally arranged σ-bonds per atom, whereas no electrons remain for any σ^*-antibonds. [25]

$$Cd(5s^2) + Se(4s^2 4p^4) \longrightarrow Cd^{2-}(5s^1 5p^3) + Se^{2+}(4s^1 4p^3)$$

In reality, mixed bonds form and the degree to which each scenario contributes to the actual condition is expressed by the *ionicity*. [24, 26]

In such direct-gap semiconductors, optical transitions take place between states with a wavenumber of $k = 0$. The **valence band maximum (VBM)** is formed by electrons in the selenium $4p$-orbitals and the **conduction band minimum (CBM)** is based on the cadmium $5s$-orbitals. [25, 27, 28]

The energy of s-electrons (azimuthal quantum number $l = 0$) at the conduction band minimum is two-fold degenerate due to the electron spin ($s = \pm 1/2$).

The valence band is in principle six-fold degenerate: the p-orbitals have an azimuthal quantum number of $l = 1$. However, because of spin-orbit coupling, the total angular momentum quantum number j can take two possible values: $j = l \pm s$. Three individual energy bands form (fig. 2.2, left), each with a distinct set of quantum numbers and a specific effective mass m^* (tab. 2.2). [29, 30]

The bands with $j = 3/2$ are called the *heavy-hole band* and the *light-hole band* because their carriers have a slightly different dispersion relation. At $k = 0$, the light-hole band has an energy that lies 25 meV (for CdSe) [23] below the heavy-hole band.

The band for $j = 1/2$ is split off at $k = 0$ by an energy $\Delta_0 = 0.42$ eV (CdSe). [23, 31]

	j	m_j	m^* / m_e	ΔE [eV]
CBM	$\pm 1/2$	0	0.11	1.74
heavy-hole band (hh)	$3/2$	$-3/2, 3/2$	1.14	0
light-hole band (lh)	$3/2$	$-1/2, 1/2$	0.31	-0.025
split-off band (so)	$1/2$	$-1/2, 1/2$	0.49	-0.42

Tab. 2.2: Band parameters for CdSe. The orbitals are characterized by a total angular momentum j and a magnetic quantum number m_j. The effective mass m^* of electrons (CBM) or holes (hh, lh, so) is given in units of the electron rest mass m_e. ΔE is the band's energy at k=0 relative to the heavy-hole band. Values from Norris *et al.* [23, 28]
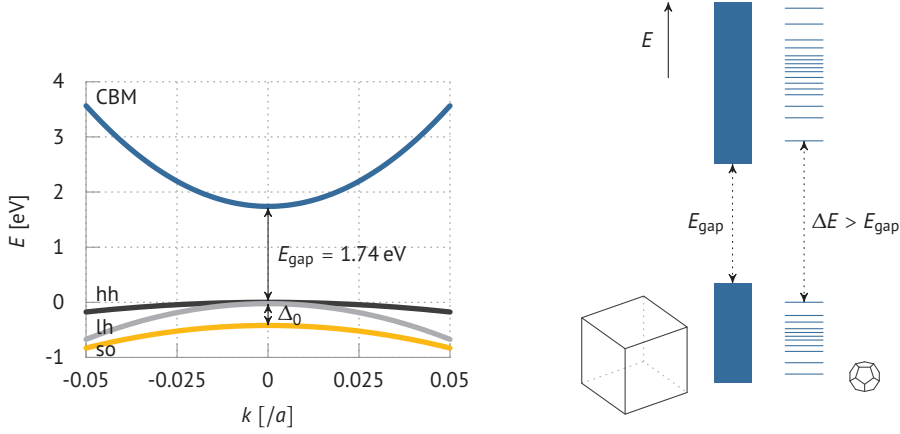
Fig. 2.2: (Left) Band structure of bulk CdSe in the close vicinity of the Γ point (k = 0) of the first Brillouin zone. The conduction band minimum (CBM) and the three distinct hole bands (hh: heavy hole, lh: light hole, so: split-off) are plotted as stated in eq. 2.7 using the values from Norris *et al.*[28] The wave number k is given in units of the inverse of the lattice constant a (tab. 2.1), which corresponds to the size of the first Brillouin zone. **(Right)** Transition from continuous energy bands in a bulk semiconductor to atomic-like energy levels in a nanocrystal as a result of the *quantum size effect.*[23] Charge carrier confinement leads to an increased gap energy.

2.1.2 Electric Conductivity and the Fermi Level

In the preceding section, energy bands have been introduced and already been called the *conduction* and *valence* band, hinting at their nature. Electric conductivity relies on charge carriers that are able to move through the material. To do so, they must be loosely bound to the nuclei or completely delocalized.

Electrons in the valence band contribute to the chemical bonds and are not able to move about freely. On the other side, electrons in the conduction band can join an electric current because they are not bound to a specific space around an atomic nucleus anymore.

Whether a material is a conductor, an intrinsic semiconductor (i.e. undoped) or an insulator is determined by the electron density in the conduction band. Since it lies energetically higher than the valence band, the degree to which it is occupied depends on the size of the energy gap E_{gap} (fig. 2.2) and on the the temperature (or, more specifically, the thermal energy of the electrons).

The Fermi-Dirac distribution for a system of identical, independent fermions gives the probability P_e that a state with the energy E is occupied by an electron:

$$P_{\text{e}}(E) = \left[\exp\left(\frac{E - \mu(T)}{k_{\text{B}} T} \right) + 1 \right]^{-1}.$$
(2.8)

This probability depends on the system's chemical potential $\mu(T)$ and its absolute temperature T.
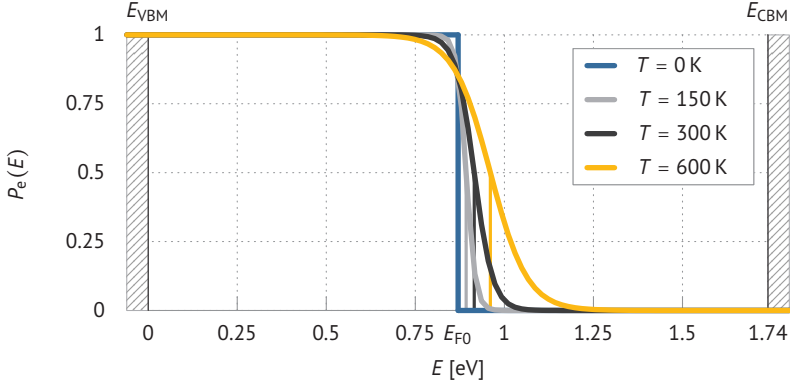
Fig. 2.3: Fermi-Dirac distributions (eq. 2.8) of CdSe heavy-hole states at four different temperatures T. $P_e(E)$ gives the probability that the state with energy E is occupied by an electron. The Fermi energy E_{F0} lies exactly halfway between the valence and the conduction band (eq. 2.11). The dashed lines mark the position of the Fermi level ($P = 0.5$). Note that for intrinsic semiconductors, no actual states exist within the energy gap between valence and conduction band.

In intrinsic semiconductors such as pure CdSe, there are no electrons in the conduction band at zero temperature (fig. 2.3). For $T > 0$, electrons from the valence band can gain enough thermal energy to accomplish the transition to the conduction band. They leave behind an *electron hole* in the valence band. Both the conduction band electron and the valence band hole participate in electric conduction, moving in opposite directions in an electric field. The Fermi-Dirac distribution for hole states P_h is exactly complementary to that of electron states:

$$P_h(E) = 1 - P_e(E) = \left[\exp\left(\frac{\mu(T) - E}{k_B T}\right) + 1\right]^{-1}. \tag{2.9}$$

The chemical potential for an intrinsic semiconductor is given by[32]

$$\mu(T) = \frac{E_{CBM} + E_{VBM}}{2} + \frac{3}{4}k_B T \ln\frac{m_h^*}{m_e^*}, \tag{2.10}$$

where E_{CBM} and E_{VBM} denote the energies of the conduction band minimum (CBM) and valence band maximum (VBM), respectively, whereas m_e^* and m_h^* are the effective masses of an electron and a hole.

At $T = 0\,K$ the Fermi-Dirac distribution (eq. 2.8) features a sharp edge: all states with an energy below μ are occupied, whereas higher energies $E > \mu(0\,K)$ are not present in the system (fig. 2.3). This specific energy $E_{F0} = \mu(0\,K)$ is called the **Fermi energy**. As can be seen from eq. 2.10, the Fermi energy for an intrinsic semiconductor lies exactly between the valence band and the conduction band:

$$E_F = \frac{E_{CB} + E_{VB}}{2}. \tag{2.11}$$
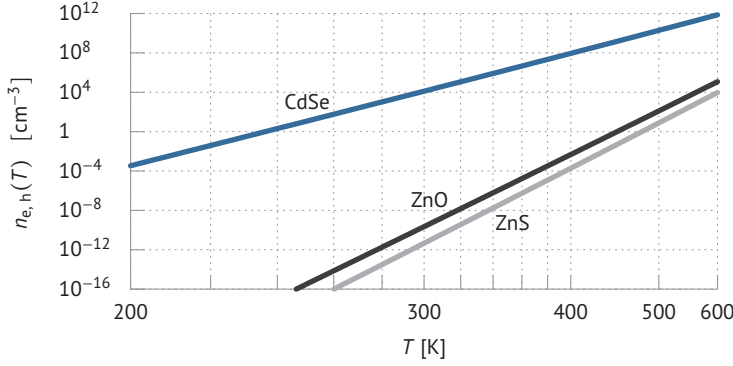
Fig. 2.4: Charge carrier densities (i.e. density of free electrons or holes) for three intrinsic semicon-
ductors that play essential roles in this thesis: CdSe (E_{gap} = 1.74 eV), ZnS (3.54 eV) and ZnO
(3.4 eV). The temperature axis is scaled like $1/T$. Effective mass values are taken from Nor-
ris[28] and Coleman.[34]

For higher temperatures, the chemical potential (eq. 2.10) increases. According to the
Fermi-Dirac distribution (eq. 2.8), an electron state with the energy $E_F = \mu(T)$ is oc-
cupied with a probability of 50 %. This characteristic energy is called the **Fermi level**.
It is shown by the dashed lines in fig. 2.3 for CdSe at different temperatures.

Because in intrinsic semiconductors the energy barrier between the Fermi level and the
conduction band minimum usually exceeds the thermal energy by one or two orders
of magnitude, the conduction band is scarcely populated at room temperature.

The density of states $g(E)$ gives the number of energy states that are available within
the energy interval $[E, E + \delta E]$. Together with the Fermi-Dirac distribution $P(E, T)$ it
can be used to calculate the charge carrier density $n(T)$ in the conduction band (for
electrons) or the valence band (for holes):

$$n_e(T) = \int_{E_{CBM}}^{\infty} g_e(E) \cdot P_e(E, T) dE, \tag{2.12}$$

$$n_h(T) = \int_{-\infty}^{E_{VBM}} g_h(E) \cdot P_h(E, T) dE. \tag{2.13}$$

Using various simplifications and neglecting any impurities, this can be solved for an
intrinsic semiconductor where the number of electrons equals the number of holes:[33]

$$n_e(T) = n_h(T) = \frac{1}{4} \left(\frac{2k_B T}{\pi \hbar^2} \right)^{3/2} (m_e^* m_h^*)^{3/4} \cdot \exp\left(-\frac{E_{gap}}{2k_B T} \right). \tag{2.14}$$

For CdSe, this leads to a charge carrier density of about $13\,000/\text{cm}^3$ at T = 300 K.
This value decreases exponentially with an increasing band gap. The band gap and
temperature dependence are shown in fig. 2.4.

2.1.3 Excitons and Confinement

When a photon with an energy higher than the band gap is absorbed, an electron can be raised from the valence into the conduction band. It leaves a hole behind. Both the electron and the hole are still bound to each other due to the Coulomb force that acts between them. From a quantum mechanical view, this bound state is a quasiparticle called an **exciton.**

The spatial extent of a particle is given by the Bohr radius a_B.[23] In analogy to the hydrogen Bohr radius a_0, it can be calculated for electrons, holes and excitons with material-specific effective masses m^* that take the place of the electron rest mass m_0. For bulk CdSe with a relative permittivity of $\varepsilon_r \approx 10$ [35] the following Bohr radii result:

$$a_B = \varepsilon_r \frac{m_0}{m^*} a_0 = \begin{cases} a_e & \approx 5\,\text{nm}, \\ a_h & \approx 1/2\,\text{nm}, \\ a_{exc} & \approx 6\,\text{nm}. \end{cases} \tag{2.15}$$

The effective mass of the exciton m^*_{exc} is given by the reduced mass of the electron and the hole: $m^*_{exc} = m^*_e m^*_h / (m^*_e + m^*_h)$.

When the quantum dot radius R reaches a size that is on the natural length scale of the electron and the hole, and the surrounding matrix material is of insulating character, the following three **confinement regimes** can be distinguished:[23, 36]

(a) *Strong confinement regime* for $R < a_h, a_e, a_{exc}$: all three particles are strongly confined and the confinement energy exceeds the Coulomb attraction. The electron and the hole can be treated separately with the Coulomb energy as a first-order energy correction.

(b) *Weak confinement regime* for $a_h, a_e < R < a_{exc}$: the individual particles (electron and hole) are considered free, but the motion of the exciton's center of mass is still confined. Coulomb attraction contributes the major part to the exciton's energy and the confinement is treated as a small disturbance.

(c) *Intermediate confinement regime* for $a_h < R < a_e, a_{exc}$: the electron and the exciton are strongly confined, whereas the hole can be considered free. Coulomb attraction and confinement energy are of the same order of magnitude.[37]

To solve the Schrödinger equation (eq. 2.2) for such confined particles, the quantum dot is approximated by a spherical potential well with an infinite energy barrier:

$$U(\vec{r}) = \begin{cases} 0 & \text{for } |\vec{r}| < R, \\ \infty & \text{for } |\vec{r}| \geq R. \end{cases} \tag{2.16}$$

This simple model is solved by any de Broglie wave that can form a standing wave within the confined region. The wavefunction consists of spherical harmonics Y_l^m, scaled by

an lth order spherical Bessel function j_l along the radial coordinate r:

$$\Phi_{n,l,m}(r,\theta,\phi) = \frac{C}{r} \cdot j_l(r\alpha_{n,l}/R) \cdot Y_l^m(\theta,\phi), \qquad (2.17)$$

where C denotes the normalization constant and $\alpha_{n,l}$ the nth zero of the Bessel function which ensures a decrease to zero at the boundary $r = R$. The energy eigenvalues increase with $1/R^2$, and the wavenumber $k_{n,l} = \alpha_{n,l}/R$ becomes quantized:

$$E_{n,l} = \frac{\hbar^2 \alpha_{n,l}^2}{2m^* R^2}. \qquad (2.18)$$

This results in discrete energy levels and an increase in the energy difference between valence band maximum and conduction band minimum (fig. 2.2, right). For this reason, quantum dots are called *artificial atoms*. In terms of molecular orbitals, the highest energy state in the valence band is now referred to as a HOMO (highest occupied molecular orbital), whereas the lowest energy state in the conduction band is a LUMO (lowest unoccupied molecular orbital).

Even though the nanocrystals cannot be considered a pure bulk anymore, their size still exceeds the lattice constant by about one order of magnitude. The wave function of a particle within a lattice potential, given by a Bloch wave (eq. 2.4), is therefore still valid. The *envelope function approximation*[23] is a good approach to combine the Bloch wave – which extends homogeneously over the whole lattice and obeys its periodicity – with an envelope wave function that takes the potential well and its boundary conditions into account. The focus is on electrons at $k \approx 0$ since this is the point where transitions between valence and conduction band take place. Therefore, only the Bloch functions $u_{n,k=0}$ need to be considered:

$$\psi(\vec{r}) = \Phi_{n,l,m}(\vec{r}) \cdot u_{n,0}(\vec{r}). \qquad (2.19)$$

For the case of strong confinement, the exciton wavefunction is treated as the product of the individual electron and hole wavefunctions

$$\psi_{\text{exc}}(\vec{r}) = \psi_{\text{e}}(\vec{r})\psi_{\text{h}}(\vec{r}), \qquad (2.20)$$

and the contribution from Coulomb attraction as an energy correction E_{C}:[25]

$$E_{\text{exc}}(n_{\text{h}}, l_{\text{h}}, n_{\text{e}}, l_{\text{e}}) = \frac{\hbar^2}{2R^2}\left[\frac{\alpha_{n_{\text{e}},l_{\text{e}}}^2}{m_{\text{e}}^*} + \frac{\alpha_{n_{\text{h}},l_{\text{h}}}^2}{m_{\text{h}}^*} \right] + E_{\text{gap}} - E_{\text{C}}. \qquad (2.21)$$

Each excitonic state is identified by a set of four quantum numbers: $n_{\text{h}}, l_{\text{h}}, n_{\text{e}}, l_{\text{e}}$. l is usually connected to s, p and d orbitals, and so the exciton's ground state is written as $1S_{3/2}1S_{\text{e}}$.[38] The Coulomb correction is of the order $E_{\text{C}} \sim e^2/\varepsilon R$.[39, 40]

2.2 Optical Properties of Colloidal Core/Shell Nanocrystals

2.2.1 Optical Transitions and Spectra

In the last section, discrete energy levels as a result of the small nanocrystal size were discussed, as well as an increase in the band gap energy due to the charge carrier confinement (fig. 2.2, right). These effects can be shown experimentally by taking absorption and emission spectra.

For an absorption spectrum (fig. 2.5), the optical density A of a sample is measured for a range of wavelengths λ or, analogously, photon energies $E = hc/\lambda$. It gives the ratio of extinction between the incident radiation intensity I_0 and the transmitted intensity I on a logarithmic scale:

$$A(\lambda) = \log_{10} \frac{I_0(\lambda)}{I(\lambda)}. \tag{2.22}$$

Any photon that causes the creation of an exciton will not be transmitted. Therefore, peaks in the absorption spectrum are connected to optical transitions within the crystal. The lower-energy transitions are usually clearly resolved (fig. 2.5) because the corresponding energy levels are well separated. The peak width is mainly the result of the sample's size dispersion, but also contains contributions from exciton fine structure splittings. [38] Higher-energy transitions take place between levels that are closer to each other (fig. 2.2, right). In the spectrum, they form a broad and increasing continuum at lower wavelengths with no resolved peaks, but clear absorption edges from the distinct hole bands. [37]

The peak heights are determined by the probability of the transition, which is proportional to the resulting exciton's electron and hole wavefunction overlap K:

$$K_{(n,l,m)_{e,h}} = \left| \int \psi_e(\vec{r})\psi_h(\vec{r})\mathrm{d}^3 r \right|^2. \tag{2.23}$$

This also allows to deduce the selection rules for transitions, as done by Ekimov *et al.* [37]

The exciton can decay by electron-hole recombination, creating a photon that carries the exciton's energy. This takes place always from the exciton's ground state $(1S_{3/2}1S_e)$. [25] When excited with energies above the band gap, such »hot« electrons and holes rapidly relax to the lowest band energy by interaction with phonons [41] and optically active vibrational modes of the ligands. [42] This process is called »cooling« and takes place on the timescale of picoseconds.

The fluorescence spectrum (fig. 2.5) shows the emission intensity as a function of the emission wavelength. For nanocrystals, it reveals that the first absorption peak is situated at higher energies than the fluorescence maximum. This effect is known for most fluorophores and called the *Stokes shift.* In the case of direct-gap semiconductor quantum dots, the electron's spin is conserved when it is raised from the valence to the conduction band. The generated hole has the opposite spin, resulting in a singlet state exciton (anti-parallel spins). Radiative recombination is allowed in this state. However,

after its generation, the exciton quickly decays to the triplet state (parallel spins),[43] which lies energetically lower due to electron-hole exchange interaction.[44] This long-lived state is optically passive: it can neither be created directly by excitation nor can it recombine solely by photon emission. This is not allowed by the quantum mechanical selection rules and it is therefore called the *dark exciton*. Deexcitation usually takes place by transferring momentum to phonons[45] before decaying radiatively. The resulting energy loss is visible in the spectrum as the Stokes shift.

The fluorescence peak's width is governed by the sample's size dispersion and spectral diffusion processes.[46]
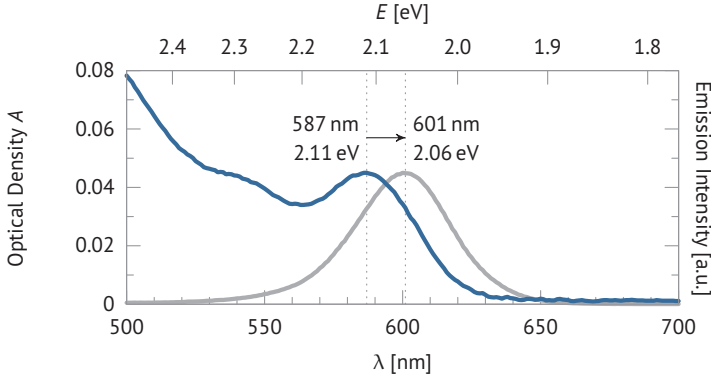
Fig. 2.5: Absorption (dashed line) and fluorescence spectrum (solid line, λ_{exc} = 470 nm) of a sample of *Fort Orange* CdSe/ZnS quantum dots from Evident Technology with a radius of $R \approx 2$ nm. The first absorption peak corresponds to the $1S_{3/2} - 1S_e$ transition. The fluorescence is subject to *Stokes shifting* (indicated by the arrow).

2.2.2 Fluorescence Intermittency: The Blinking Phenomenon

One of the most interesting and yet not fully understood properties of colloidal quantum dots is their specific fluorescence intermittency.[14] Under (continuous) excitation, their luminescence response switches abruptly between »on« states with a bright signal and »off« states with a very low signal, or none at all, whereas the absorption stays at a constant value. This behavior is commonly called »blinking« and found for many nanoscale fluorophores,[15] including single molecules and nanorods. Intermediate signal states and even continuous distributions of emission states are also observed for CdSe/ZnS quantum dots.[16] A typical nanocrystal fluorescence time trace is shown in fig. 2.6.

When threshold values are applied to distinguish between »on« an »off« states, their individual duration τ can be measured. This reveals an inverse power law distribution for both »on« and »off« durations over at least seven orders of magnitude in time:[47]

$$P_{\text{on, off}}(\tau) \propto \tau^{-\alpha_{\text{on, off}}}. \tag{2.24}$$

The observed »on« and »off« times τ range from about 100 µs up to several minutes and
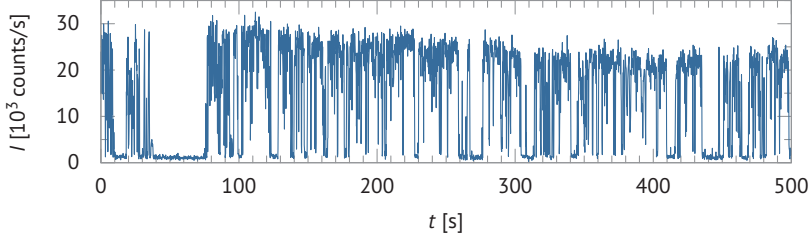
Fig. 2.6: Fluorescence time trace of a single quantum dot on glass in air. The typical fluorescence intermittency is seen from distinguished »on« and »off« states in the signal. Data collected using confocal microscopy and an avalanche photo diode for time-tagged, time-resolved single photon counting.

are apparently only limited by the time resolution that can be realized experimentally. These time scales are much longer than the intrinsic times of quantum mechanical processes, which implies a switching mechanism between metastable »on« and »off« states.

The »on« time distribution of quantum dots typically features a cut-off around the order of $\tau_{\text{cut, on}} \approx 1 \ldots 10\,\text{s}$; longer »on«-times are suppressed. This truncation point depends on the temperature, excitation power, shell thickness[48] and the dielectric constant of the surrounding medium.[19] For the »off« times, such cut-offs are found for durations one order of magnitude longer: $\tau_{\text{cut, off}} \approx 10 \ldots 100\,\text{s}$.[19]

The behavior after the cut-off can be fit by a superimposed exponential decay:

$$P_{\text{on, off}}(\tau) \propto \tau^{-\alpha_{\text{on, off}}} \cdot e^{-\beta\tau}. \tag{2.25}$$

The »off« state is most generally seen as a state with a high non-radiative decay rate Γ_{nr} of the exciton, whereas in the »on« state, both the radiative rate Γ_{r} and the non-radiative one are of the same order of magnitude. Such rate fluctuations have an effect on the overall **quantum yield η,** which gives the ratio of excitons decaying radiatively to the total number of absorbed photons:

$$\eta = \frac{\Gamma_{\text{r}}}{\Gamma_{\text{nr}} + \Gamma_{\text{r}}}. \tag{2.26}$$

The non-radiative rate is known to be influenced by charges within the quantum dot core or on its surface.[19] This discovery gave rise to several interpretations of the »off« state, the most prominent ones being an increase of the non-radiative rate due to Auger processes and the filling or clearance of hole or electron traps. The next section will introduce these exciton relaxation mechanisms in more detail.

2.2.3 Nonradiative Relaxation Mechanisms

Apart from the aforementioned radiative recombination of electron and hole (section 2.2.1 and fig. 2.7a) which results in the typical fluorescence of a quantum dot, there are several relaxation pathways that don't lead to the emission of photons. Each of these decay channels has a characteristic lifetime τ: the mean time (exponential distribution) that a charge carrier stays in the excited state until it relaxes via the decay channel. The channel's effective relaxation rate is therefore $\Gamma = 1/\tau$. All of the decay channels contribute to the overall nonradiative rate Γ_{nr}, which leads to fluorescence quenching, i.e. a decrease in the quantum yield η (eq. 2.26).

(a)	(b)	(c)
Radiative Recombination	Phononic Cooling	Energy Transfer to Hole
$\tau \sim 10\,\text{ns}$	$\tau > 200\,\text{ps}$	$\tau < 1\,\text{ps}$
(d)	(e)	(f)
Negative Trion (Auger)	Positive Trion (Auger)	Trapping
$\tau \sim 100\,\text{ps}$	$\tau \sim 100\,\text{ps}$	$\tau \sim 1\,\text{ps}$
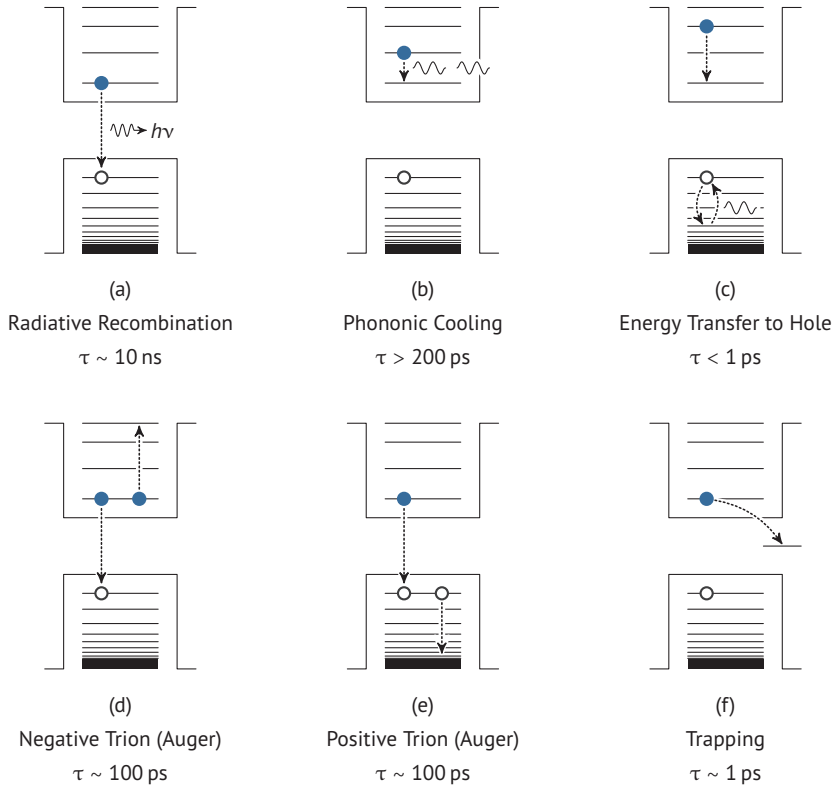
Fig. 2.7: Relaxation mechanisms for excitons in semiconductor nanocrystals. Typical relaxation lifetimes τ are listed for room temperature.

Charge Carrier Cooling via Phonons

In bulk semiconductors, excited electrons and holes can easily relax to the lowest energy states of their respective bands by interacting with the lattice and thus creating longitudinal optical (LO) phonons. However, in quantum dots the discrete levels of the conduction band electrons feature energy differences which are too high to allow

for the creation of LO phonons one at a time: $\Delta E >> \hbar\omega_{\text{LO}}$.[49] Multiple LO phonons would need to be created for each relaxation step (fig. 2.7b), which is a highly unlikely process. The relaxation time τ_{c} of a hot carrier increases exponentially with the level spacing ΔE:[50]

$$\tau_{\text{c}} \sim \omega^{-1} \exp\left(\Delta E / k_{\text{B}} T\right), \tag{2.27}$$

where ω denotes the phonon frequency. This lead to the assumption that systems where the confinement of the exciton leads to discrete energy levels would generally feature a *phonon bottleneck*, i.e. slow intraband relaxation of hot carriers.

The lifetime of the phononic cooling has been experimentally determined to be of the order of 200 ps at room temperature.[51] However, the intraband relaxation of hot electrons and holes shows an additional, much faster component of less than a picosecond,[51] bypassing the phonon bottleneck. Experimental evidence suggests that owing to the strong wavefunction overlap, the electron's energy is transferred to the hole, which can relax much better via phonons because of its higher density of energy states.[51, 52, 53] The energy transfer from one charge carrier to another takes place by means of an Auger-like process,[54] which will be discussed in the following section.

Auger Processes

When two or more charge carriers are confined to a small space such that their Coulomb interaction is enhanced significantly, it is possible for one carrier to relax to a lower energy state by transferring energy to another carrier. This effect is called an Auger process and can be found in atoms (where it is useful in spectroscopic applications[55]) as well as for excited charge carriers in quantum dots.

In the traditional meaning of the Auger process, the energy transfer takes place between two electrons (at positions $\vec{r}_1$ and $\vec{r}_2$) through a Coulomb interaction V:[56]

$$V(\vec{r}_1, \vec{r}_2) = \frac{e^2}{\varepsilon_{\text{r}} |\vec{r}_1 - \vec{r}_2|} \exp\left(-\frac{|\vec{r}_1 - \vec{r}_2|}{r_{\text{s}}}\right), \tag{2.28}$$

where ε_{r} means the material's dielectric constant and r_{s} the Debye length (screening length). This Coulomb interaction V can be regarded as a perturbation of the system and according to Fermi's Golden Rule, there is the following transition probability W from the intial state i, expressed by the two-electron wave function $\Psi_{E_1, E_2}(\vec{r}_1, \vec{r}_2)$, to the final state f:[56]

$$W_{i \to f}^{\text{Auger}} = \frac{2\pi}{\hbar} \left|\langle \Psi_{E_1, E_2}(\vec{r}_1, \vec{r}_2) | V(\vec{r}_1, \vec{r}_2) | \Psi_{E_r, E_A}(\vec{r}_1, \vec{r}_2)\rangle\right|^2 \rho_{\text{f}}(E_A). \tag{2.29}$$

In this notation, E_{r} means the energy state of the remaining electron (with a decreased energy), whereas E_{A} denotes the one of the Auger electron which – in the traditional sense – leaves the system with a velocity that corresponds to the energy $E_A = E_1 + E_2 - E_{\text{r}}$. The density of final states for the Auger electron is expressed by the term ρ_{f}.

In the case of quantum dots, the Auger electron usually does not leave the nanocrystal

completely, but is assumed to remain in the quantum dot's core or settle at a localized state on its surface. There are several scenarios for Auger processes in quantum dots, involving multiexcitons and charged crystals (fig. 2.7d, e). Since the Auger transition is much faster than radiative recombination, it is the dominant relaxation pathway when a quantum dot is either charged or features more than one exciton. This leads to a strong decrease in the quantum yield and radiative lifetime. In the case of multiple excitons, *antibunching* can be observed, which means that the quantum dot usually emits only one photon at a time instead of in bunches: just the last remaining exciton decays radiatively.

As can be seen from equation 2.28, the Auger transition rate (eq. 2.29) strongly depends on the wave function overlap and therefore on the space to which the charge carriers are confined. Kharchenko and Rosen[56] derived that the Auger rate strongly scales inversely with the Bohr radius a_B (eq. 2.15), and hence with the nanocrystal's radius:

$$W^{Auger} \sim \frac{1}{(k_A a_B)^7}. \tag{2.30}$$

k_A is the wave number of the Auger electron (the one that gained energy), which relates to its final energy state via the material's electron dispersion relation (eq. 2.7).

Charge Carrier Trapping

Charge carriers can become trapped in highly localized energy states that arise from faults in the lattice structure or the surface. In the nanocrystals, a lattice mismatch is expected at the CdSe–ZnS interface. Even though they are both type II-VI semiconductors, the core and shell materials have different lattice constants (tab. 2.1), which leads to a lattice reorganization at the interface and new energy states. The surface of the shell is usually capped with ligands that saturate dangling bonds. In the case of this work, the nitrogen atoms of the HDA molecules have a lone electron pair that coordinates with the unsaturated Zn sites at the surface. However, the ligand coverage is incomplete and unsaturated, »dangling bonds« present energy states where charge carriers can become trapped.[25, 57] Their energies are usually located within the semiconductor band gap.[58]

Jasieniak and Mulvaney showed that a change in surface stoichiometry, i.e. the ratio of Cd and Se atoms at the surface, dramatically changes the fluorescence behavior of CdSe quantum dots.[59] Crystals with a Cd rich surface showed high luminescence, whereas more Se atoms and therefore more unsaturated electron pairs at the surface lead to a decrease in the quantum yield.

2.2.4 Excited State Lifetime

As any fluorophore being excited, quantum dots spend a certain time in the excited state before a relaxation to the ground state takes place through any of the aforementioned decay channels. In the ideal case, the sample is excited by an infinitely short δ pulse

of light. At this point, a number $N_0 = N(t = 0)$ of the quantum dots is in the excited state. The probability to decay in a given range of time is the same for each quantum dot, which means that the total number of excited quantum dots decreases exponentially:

$$\frac{\mathrm{d}N(t)}{\mathrm{d}t} = -(\Gamma_\mathrm{r} + \Gamma_\mathrm{nr})N(t) \quad \rightarrow \quad N(t) = N_0 \exp\left(-t/\tau\right). \tag{2.31}$$

The decay constant $\tau = 1/(\Gamma_\mathrm{r} + \Gamma_\mathrm{nr})$ is called the **average excited state lifetime** and describes the time after which the number of excited quantum dots drops to $N_0/e \,\hat{=}\,$ 37 %. Assuming that each quantum dot emits one photon if it decays radiatively, and the ratio of radiative to nonradiative decays stays constant, the fluorescence intensity is proportional to the decay speed:

$$I(t) \propto -\frac{\mathrm{d}N(t)}{\mathrm{d}t} \propto N(t). \tag{2.32}$$

This means that the time behavior of the fluorescence intensity measured after the pulse can be used to determine the average lifetime τ, as equation 2.31 can be rewritten as

$$I(t) = I_0 \exp(-t/\tau). \tag{2.33}$$

The lifetime is typically measured by accumulating the fluorescence response for many consecutive pulses. This technique allows the evaluation of the lifetime of a single fluorophore unit, such as a single quantum dot.

Multiexponential Decays

Often, the fluorescence does not follow a single exponential decay law, but rather a sum of individual decays:

$$I(t) = \sum_{i=1}^{M} A_i \exp\left(-t/\tau_i\right). \tag{2.34}$$

The idea is that the ensemble of fluorophores is composed of a number M of subsets with distinct radiative and non-radiative rates, and therefore individual lifetimes τ_i. To express each subgroup's absolute contribution C_i to the total fluorescence signal, its component needs to be integrated:

$$C_i = \int_0^\infty A_i e^{-t/\tau_i} \mathrm{d}t = A_i \tau_i. \tag{2.35}$$

The fractional contribution f_i of each component can then be calculated by normalization to the overall intensity:[60]

$$f_i = \frac{C_i}{\sum_i A_i \tau_i}. \tag{2.36}$$

2.3 Fundamentals of Electrochemistry

2.3.1 Redox Potentials

Redox reactions are an important class of chemical reactions found in nature and are the subject of all electrochemical investigation methods. They involve the transfer of one or more electrons between two reactants, from an electron donor *D* to an electron acceptor *A*. The process of donating an electron is called oxidation: the participant's oxidation number rises. The acceptor undergoes a process called reduction: its oxidation number is being lowered.

$$D \longrightarrow D^+ + e^- \qquad \text{Oxidation} \qquad (2.37)$$

$$A + e^- \longrightarrow A^- \qquad \text{Reduction} \qquad (2.38)$$

$$D + A \rightleftharpoons D^+ + A^- \qquad \text{Redox Reaction} \qquad (2.39)$$

A redox reaction takes place at a certain redox potential E^0, which can be seen as the electrochemical potential of the exchanged electrons. A system with a higher redox potential usually acts predominantly as an electron acceptor when in contact with a system that has a lower redox potential, which in turn acts as the electron donor. A simple example is the Daniell cell, which consists of two half-cells that are based on the redox reactions of copper and zinc, respectively:

$$Cu \rightleftharpoons Cu^{2+} + 2\,e^- \qquad E^0 = +0.35\,\text{V vs. SHE,} \qquad (2.40)$$

$$Zn \rightleftharpoons Zn^{2+} + 2\,e^- \qquad E^0 = -0.76\,\text{V vs. SHE.} \qquad (2.41)$$

When charge transfer is allowed between the two half-cells, Zn is being oxidized to Zn^{2+}, leaving two electrons for the reduction of Cu^{2+} to elementary Cu. The direction of each reaction therefore depends on the relation of the redox potentials E^0 to each other.

The redox potential of a reaction cannot be determined independently, but only compared to another redox potential. In the given example of the Daniell cell, a voltage $U = 1.11\,\text{V}$ can be measured between the two half-cells, which is the difference between the two redox potentials of the reactants. Usually the redox potential of a redox system is given in reference to the standard hydrogen electrode (SHE), where hydrogen and its ions make up the redox system:

$$H_2 \rightleftharpoons 2\,H^+ + 2\,e^- \qquad E^0 = \pm 0\,\text{V vs. SHE.} \qquad (2.42)$$

In this context, a system's redox potential expresses its ability to either oxidize H_2 molecules ($E^0 > 0\,\text{V vs. SHE}$) or reduce their H^+ ions ($E^0 < 0\,\text{V vs. SHE}$).

For each half cell, the Nernst equation relates the concentrations of oxidized (c_{Ox}) and reduced species (c_{Red}) to the actual electrode potential E:

$$E = E^0 + \frac{RT}{z_e F} \ln \frac{c_{Ox}}{c_{Red}}. \qquad (2.43)$$

The number of electrons transferred per reaction is denoted by z_e. R is the gas constant, T the absolute temperature, and F the Faraday constant.

When a voltage is applied to a metal electrode relative to another fixed reference electrode, its Fermi level E_F rises. This is equivalent to a rise in the electrode potential, which means that the Nernst equation (eq. 2.43) can as well be used to calculate the ratio of oxidized and reduced species under equilibrium conditions:

$$E_F = E^0 + \frac{RT}{z_e F} \ln \frac{c_{Ox}}{c_{Red}}. \tag{2.44}$$

In the frame of this work, the oxidized and reduced species will be semiconductor nanocrystals adsorbed to the electrode, and several stages of oxidation and reduction are conceivable:

$$QD^{2+} + 2\,e^- \rightleftharpoons QD^+ + e^- \rightleftharpoons QD \rightleftharpoons QD^- + h^+ \rightleftharpoons QD^{2-} + 2\,h^+. \tag{2.45}$$
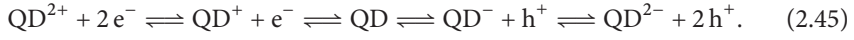
2.3.2 Semiconductor Electrochemistry

For an intrinsic semiconductor, the Fermi level is usually found within the band gap half way between the valence band maximum and conduction band minimum. At room temperature, the number of thermal electrons in the conduction band is negligible (see section 2.1.2). However, for the experiments in this work, ITO and ZnO—both natural n-type semiconductors—will be used for the working electrode that has the nanocrystal sample adsorbed to its surface. They feature a high ratio of ionic bonds, which lead to Tamm states close to the conduction and valence band edges.[58, 61] Additionally, dangling bonds at the surface usually lead to energy states located around the center of the band gap, so-called Shockley states.[58, 61] For undoped ZnO films, a conduction band electron concentration in the range of $10^{17} \ldots 10^{21}$ cm^{-3} has been found at room temperature,[62] for ITO in the range of $10^{20} \ldots 10^{21}$ cm^{-3}.[63]

The high concentration of electrons close to the conduction band due to strong natural or artificial n-type behavior leads to a relocation of the Fermi level E_F into the region close to the conduction band edge (fig. 2.8).
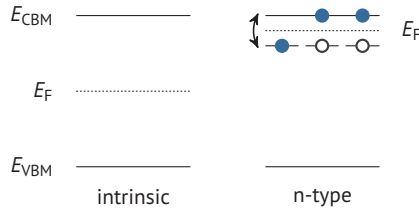
Fig. 2.8: Additional electron states close to the conduction band lead to a relocated Fermi level E_F in n-type semiconductors as opposed to the intrinsic state of a pure semiconductor.

Figure 2.9a shows the individual energy levels of an n-type semiconductor electrode and the electrolyte solution as long as they are not in contact with each other. The

Fermi level E_F in the semiconductor and the electrolyte's redox potential E_F^0, which is equivalent to its Fermi level,[64] are found at distinct values that differ from each other.

Once in contact, the Fermi levels of both materials will align (fig. 2.9b) to a common level. This equilibration takes place by electron transfer from the semiconductor to molecules in the electrolyte solution, which are usually adsorbed to the semiconductor surface and which are being reduced in the process. As electrons from near the semiconductor surface are transferred across the interface into the solution, a depletion layer—or space-charge region (SC)—forms underneath the surface. Devoid of conduction band electrons, it is dominated by the positive charges from the atomic nuclei that remain in the lattice. Consequently, a voltage U_{SC} between the surface and the bulk region of the semiconductor builds up, which counteracts the electron depletion. The width W of the space-charge region usually shows values in the range of 10...1000 nm and is dependent on the charge carrier density n_e of the semiconductor:[64]

$$W = \sqrt{\frac{2\varepsilon_r\varepsilon_0}{en_e}U_{SC}}.\qquad(2.46)$$

The result is a bending of the band potentials close to the surface. Once a dynamic equilibrium is reached, the Fermi level on both sides of the interface takes the value $E_{F,\,eq}$ and the electron transfer rate is the same in both directions. The region of adsorbed molecules on the electrolyte side of the interface where the negative charges built up in the process of Fermi level equilibration is called the »inner Helmholtz layer« (IHL). Compared to the space charge layer, it is typically very thin in the range of 0.4 ...0.6 nm. [64]
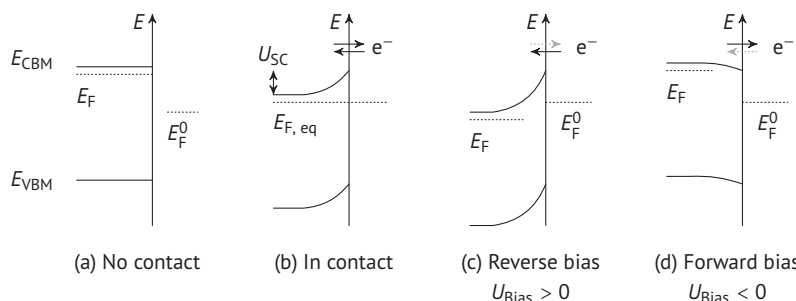
Fig. 2.9: The alignment of energy levels in a semiconductor (left of axis) and electrolyte (right). E_F illustrates the Fermi level in the respective medium. In **(a)** both are separated from each other and in **(b)** they are in contact. In **(c)** the situation is shown for a reverse bias voltage applied to the semiconductor, whereas in **(d)** a forward bias voltage is applied. Pictures adopted from Rajeshwar.[64]

In the bulk electrolyte solution, which usually hosts a high salt ion concentration, the mean charge is neutral. With the accumulation of negative charges in the inner Helmholtz layer, a potential gradient is present in the solution close to the electrode. This leads to a higher local density of positively charged ions in the region directly adjacent to the IHL, called the »outer Helmholtz layer« (OHL). Both Helmholtz layers screen the bulk electrolyte solution from the electrode potential and suppress any long-range electric

fields. This screening is characterized by the effective Debye length L_D, after which the field strength is considered noneffective. For ions that carry only one charge it is given by:[65]

$$L_D = \sqrt{\frac{\varepsilon_r \varepsilon_0 k_B T}{2e^2 c_0}},$$ (2.47)

where c_0 represents the number density of ions in the solution. Higher concentrations of salt ions lead to a more effective screening and therefore to a smaller Debye length.

In the equilibrium situation illustrated in fig. 2.9b, the electron transfer rates between semiconductor and Helmholtz layer are equal in forward and reverse direction and the net current is zero. Applying an external »bias« potential alters this balance. In the case of a reverse bias (fig. 2.9c) electrons are drawn from the electrode's conduction band, which leads to an extension of the space-charge layer. In this situation, electron ejection from the electrode becomes less likely and oxidation processes in the Helmholtz layer are favored. In the opposite case, when a forward bias potential is applied (fig. 2.9d), the electron transfer from the Helmholtz layer into the semiconductor is suppressed, and reduction processes are favored. The net current i_c through the electrode depends on the difference between the equilibrium charge carrier density n_s at the electrode surface and the density $n_{s, Bias}$ under bias conditions:[64]

$$i_c = -eAk_{et}c_{Ox}(n_{s, Bias} - n_s),$$ (2.48)

with the electrode surface area A, the electron transfer rate constant k_{et}, and the concentration of oxidized species c_{Ox}, i.e. electron accepting sites, in the inner Helmholtz layer. The concentration of electrons in the surface region is determined by bulk conduction band electrons (concentration n_e) that have the thermal energy to overcome the barrier caused by the band bending:

$$n_s = n_e \exp\left(-\frac{eU_{SC}}{k_B T}\right),$$ (2.49)

$$n_{s, bias} = n_e \exp\left(-\frac{e(U_{SC} + U_{Bias})}{k_B T}\right).$$ (2.50)
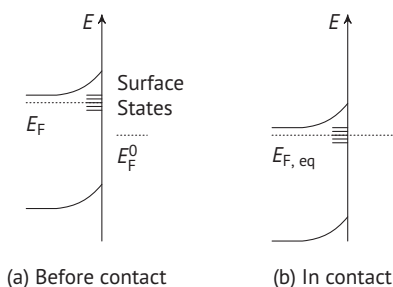
Surface States and Fermi Level Pinning

When the redox potential E_F^0 of the electrolyte is situated further below the conduction band, at energies around the center of the band gap, reduction and oxidation can be strongly inhibited because of the very high energy barrier that needs to be overcome from both sides. However, mid-gap energy states that arise from unsaturated bonds at the electrode surface (Shockley states) present a means to bypass this energy barrier. They can act as transfer channels between the semiconductor bands and the electrolyte.[58]

Semiconductor surface states can be occupied with electrons from the bulk. This leads to a higher concentration of negative charges at the surface, and a depletion layer right

below. As a result, the Fermi level E_F is pinned to these surface states and the semiconductor shows band bending even before contact with an electrolyte.[61] This situation is illustrated in fig. 2.10a.

Once the semiconductor is in contact with an electrolyte, the charge transfer mostly takes place through the surface states (fig. 2.10b). The energy barrier in the conduction band itself stays constant because the bulk and surface concentrations of electrons remain the same. Only the energies align until they match the electrolyte's redox potential E_F^0.

The degree of Fermi level pinning depends on the concentration of surface states. Situations between no pinning and complete pinning are possible.


(a) Before contact   (b) In contact

Fig. 2.10: (a) In the presence of many electron-occupied surface states the Fermi level E_F in the semiconductor will be pinned to the energy of these states. As the result of charge accumulation, the band bending and related charge barrier will establish even before contact to the electrolyte. **(b)** In contact with the electrolyte, the charge carrier exchange takes place mostly through the surface states. The band edge energies are pinned to the Fermi level. Pictures adopted from Memming.[61]

2.3.3 Cyclic Voltammetry

When redox reactions take place at an electrode under a bias voltage U_{Bias}, the redox equilibrium is off balance, resulting in a non-zero net current that can be measured. Voltammetric analysis methods measure the current in response to the applied bias voltage.

In cyclic voltammetry (CV), the electrode voltage U (usually in reference to another electrode) is scanned in a triangular pattern through a specific potential region (fig. 2.11a). The potential changes linearly in time with the scan rate $v = \Delta U / \Delta t$ until one of the reversal potentials U_{high} or U_{low} is reached. At these points, the scan rate changes its sign and therefore the scan's direction.

In dynamic equilibrium, as long as the electron transfer takes place on a faster timescale than the scan rate, the concentration of oxidized and reduced species in the solvent near the interface is given by the Nernst equation (eq. 2.44). Conversely, in the bulk away from the electrode both redox species have equal number densities. Since the Helmholtz layer screens the bulk from the charges at the electrode, any current flowing to or from the electrode is only determined by the diffusion in the solution, as this is
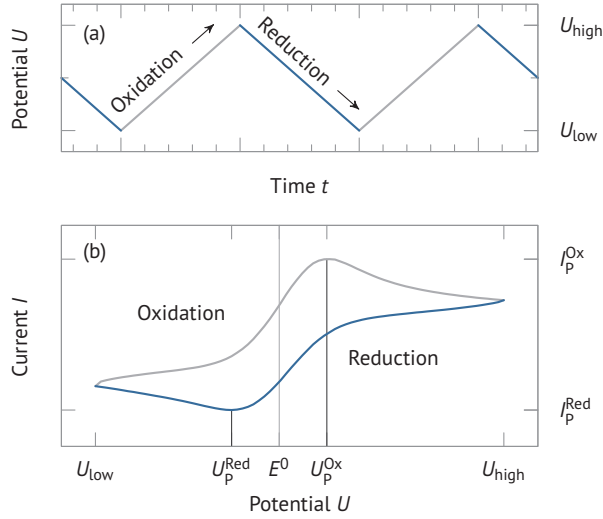
Fig. 2.11: (a) Time trace of the voltage U as the bias potential at the electrode is changed in a triangular pattern, resulting in electrode potentials between U_{high} and U_{low}. Oxidation (gray) and reduction sweeps (blue) are characterized by the scan direction. **(b)** The voltammogram for a single redox couple shows the current I through the electrode in dependence on the applied potential U. Peak potentials U_P^{Red}, U_P^{Ox} and peak currents I_P^{Red}, U_P^{Ox} are labeled for their individual sweeps. E^0 denotes the redox potential. Colors as in (a).

the only process that transports reactant molecules between the electrode and the bulk. Therefore, the flux J of reactant is driven by the concentration gradients, i.e. Fick's law:

$$J_i = -D_i \nabla c_i, \tag{2.51}$$

where D_i is the diffusion coefficient and ∇c_i the concentration gradient of the redox partner i in question—i.e. either the oxidized or reduced species. The current through the electrode is then given by

$$I = z_e e A D \left[\frac{\partial c_{Ox}}{\partial x} \right]_{x=0} = -z_e e A D \left[\frac{\partial c_{Red}}{\partial x} \right]_{x=0}, \tag{2.52}$$

where z_e is the number of electrons transferred per reaction. A denotes the electrode surface, and D the diffusion coefficient, assuming the oxidized and reduced species have mostly the same effective radius in the solvent. The condition $c_{Ox} + c_{Red} = \text{const.}$ must hold true. The two gradients are therefore complementary.

Measuring the current throughout a complete scan cycle and plotting it over the applied potential results in a voltammogram as illustrated in fig. 2.11b. At the lower reversal potential U_{low} the reduction is highly favored, and only reduced species will be present at the electrode:

$$\text{Ox} + \text{e}^- \longrightarrow \text{Red.} \tag{2.53}$$

Once the oxidation sweep starts and the voltage approaches higher potentials, the oxidation rate will begin to increase as the oxidation potential is approached. Reduction will still strongly take place as long as the potential stays in the region of the reduction potential. Only when reduction becomes less likely, the current strongly increases. The net current I through the electrode will change its sign when both oxidation and reduction are equally favored:

$$Ox + e^- \rightleftharpoons Red. \qquad (2.54)$$
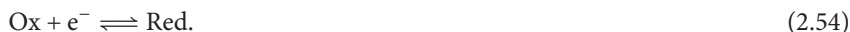
The current further increases as the oxidation direction becomes stronger and the reduction less likely. Once all molecules at the electrode are oxidized, the current reaches a peak at U_p^{Ox}. At this point, the Helmholtz layer adjacent to the electrode becomes depleted of reduced species molecules and the diffusion flux from the bulk cannot keep up with the rate of oxidation anymore. This leads to a decrease in the current.

At the upper reversal potential U_{high} the oxidation is highly favored and only oxidized species is present at the electrode:

$$Ox + e^- \longleftarrow Red. \qquad (2.55)$$

As the scan direction is reversed, all the aforementioned processes will take place again in an inverted manner: at first, oxidation is still favored, but as the reduction becomes more likely, the current will decrease again until it reaches a peak in the other direction at U_p^{Red} and only reduced species will be found at the electrode.

An increase of the scan rate v will lead to an increase in the peak currents. Because the change in concentration at the electrode is more rapid, this will lead to a stronger concentration gradient and thus to a higher current. When the peak potentials U_p^{Ox} and U_p^{Red} are independent of the scan rate, this means that electron transfer between the electrode and the reactants takes place very quickly and is not delayed with respect to the scan rate. Theory predicts that the two peaks will be separated by $\Delta U_{Peak} = (59/z_e)$ mV from each other, where z_e is the number of electrons transferred per reaction. [66] This ideal scenario is called *reversible electron transfer*.

Slow transfer rates, however, will lead to oxidation and reduction rates that are too slow to establish the concentration ratios required by the Nernst equation (eq. 2.44). This delay can be seen in a bigger peak separation with increasing scan rates v. This situation is called *quasi-reversible* or *irreversible*.

For symmetric peak behavior, the potential E^0 in the center between the two peaks represents the redox potential.

3 Experimental Basics and Evaluation Techniques

3.1 Quantum Dots: The Objects under Investigation

The semiconductor nanocrystals used for this work were produced by Evident Technologies and sold under the trademark *EviDots*. They are colloidal particles of spherical shape, consisting of a CdSe core with a diameter of ca. 4 nm[67] that is capped with ≈ 2 monolayers of ZnS (fig. 3.1), which leads to a shell thickness of ≈ 0.6 nm.[68] The fluorescence emission maximum is at $\lambda_{em} \approx 601$ nm, with a slight dependence on the environment. The manufacturer calls this size choice *Fort Orange*.

The ZnS capping layer is meant to passivate the dangling bonds at the core's surface and leads to a significantly higher quantum yield.[69] Further passivation is achieved with hexadecylamine (HDA) ligand molecules attached to the quantum dot surface, which have a fully extended length of ≈ 2.2 nm.[70] For a detailed picture of the surface–ligand coordination, see fig. 1.1 in the introduction.

The nanocrystals come solved in toluene with a mass concentration of $\beta_{QD} = 5$ mg/ml, which translates to a molar concentration of $c_0 \approx 14$ nmol/ml, as verified by absorption spectroscopy using the Beer-Lambert law. The solution also contains HDA in a concentration such that a sufficient surface passivation is maintained by a dynamic equilibrium of ligand adsorption and desorption.[71]

3.2 Optical Detection Methods

3.2.1 Fluorescence Microscopy

In general, fluorescence microscopy methods are based on the excitation of a fluorophore at a wavelength that is smaller than the wavelength of the fluorescence light, which allows to easily separate them. For all time-tagged measurements, a Hamamatsu C8898 pulsed laser diode is used in this work to generate short light pulses of 88.67 ps pulse width at frequencies in the range of $1\ldots10$ MHz, at a wavelength of $\lambda_{exc} = 470$ nm. This wavelength is suitable because the quantum dots show a broad absorption spectrum in this region (see fig. 2.5) and it is sufficiently off the fluorescence wavelength at $\lambda_f = 601$ nm.
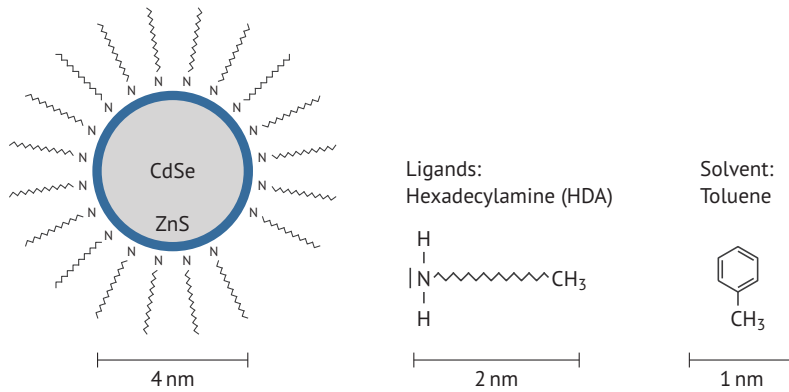
Fig. 3.1: The quantum dots consist of a CdSe core capped with a ZnS shell. They have a diameter of 4 nm with a very narrow size distribution. Attached to the surface are HDA ligands of ca. 2 nm length, yet the surface coverage cannot be assumed to be complete. The quantum dots are solved in toluene.

The sample holder is mounted to an XYZ nanopositioning stage (PI P-517.3C) that is controlled with a Labview program. An oil immersion objective (Olympus UPlanSApo 100×, NA = 1.4) is used for all measurements, both for directing the excitation light onto the sample and for collecting the luminescence light from the sample. To separate it from residual excitation light, a dichroic mirror is used in combination with a long pass filter that transmits wavelengths $\lambda > 502$ nm (Omega Optical 502ALP).

A common optical microscope is based on the observation of light reflected by or transmitted through the sample. Its resolution is limited by diffraction. The distance d between two objects at which they can still be discerned is described by the Rayleigh criterion and depends on the wavelength λ of the light that is directed onto the sample and the numerical aperture NA of the objective lens:

$$d = \frac{0.61\lambda}{\text{NA}}. \tag{3.1}$$

The numerical aperture is given by $\text{NA} = n\sin(\alpha/2)$, where n is the refractive index of the immersion medium and α the angular aperture of the objective. Fluorescent particles provide a convenient means to circumvent this limit, as described in the following section.

3.2.2 Confocal Fluorescence Microscopy

The principle of confocal microscopy is to use a very small excitation volume to observe only very few, or even single fluorophores. The setup used here is illustrated in fig. 3.2. Parallel beams of light are directed into the objective and focused in one point directly on the sample. The fluorescence from this very narrow focal volume then leaves the objective as a beam of parallel light, is filtered from residual excitation and background light by the dichroic mirror and the long pass filter mentioned in the previous section,

and is then focused onto a pinhole (50 μm diameter). Only light from the focal plane will be in focus at the pinhole. Any background light that originates from outside this plane will be highly defocused at the pinhole and therefore reliably cut off. The signal is then separated into two perpendicular, linearly polarized components before being directed onto two avalanche photo diodes (Picoquant MPD PDM series) for time-tagged, time-resolved single photon detection. The pulses triggered by single photons are processed by a counting card (Becker & Hickl DPC230) and passed on to the computer software as time-tagged events.

This technique leads to a slightly better in-plane resolution:[72]

$$d_{xy} = \frac{0.44\lambda}{\text{NA}}.$$ (3.2)

One drawback is the inability to observe a larger sample area at once. This is partly compensated for by scanning the microscope objective over the sample and accumulating a picture by position-resolved intensity detection.
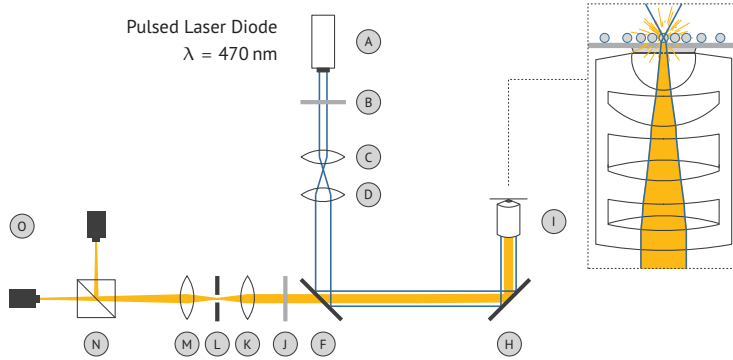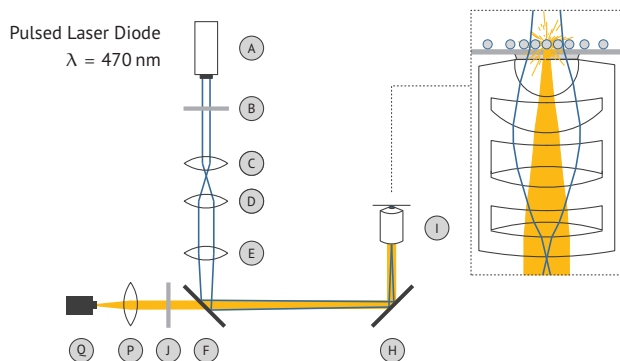

Fig. 3.2: Schematic of the confocal microscope setup. The excitation beam (blue line) from a pulsed laser diode **(A)** is directed through a laser line filter **(B)** and a beam expander **(C, D)** before it is reflected at a dichroic mirror **(F)** and a regular mirror **(H)** into an oil immersion objective **(I)**. It enters the objective as a parallel beam and is forwared onto the quantum dot sample, where it excites single quantum dots in the very narrow focal volume. The fluorescence response from the nanocrystals (yellow line) returns on the same way to the dichroic mirror, which is transmissive for the fluorescence wavelength of the quantum dots. After a long pass filter **(J)** and a pinhole setup **(K, L, M)** it is separated into two linearly polarized (perpendicular) components with a polarizing beam splitter **(N)** and finally detected by two avalanche photo diodes **(O)**.

3.2.3 Time-Resolved Ensemble Detection

To facilitate time-tagged, time-resolved single photon analysis of a large quantum dot ensemble and to record more data, the confocal setup described in the previous section can be altered towards wide-field excitation. The corresponding setup is shown in fig. 3.3. The excitation light is focused into the back focal plane of the objective, resulting in a wide, parallel beam on the sample side. The detected light still leaves the objective in a parallel beam, but contains the fluorescence signal from an ensemble region that

measures about 10 μm in diameter. This light is again filtered and then focused onto a single avalanche photo diode (PerkinElmer SPCM-AQR-13).

Fig. 3.3: Schematic of the time-resolved ensemble detection setup. In difference to the confocal microscopy setup (fig. 3.2), the excitation beam is here focused by an additional lens **(E)** into the back focal plane of the objective, which leads to a wide-field illumination. The fluorescence signal from the much bigger excitation area (ca. 10 μm in diameter) is focused through a lens **(P)** onto a single avalanche photo diode **(Q)**.

3.2.4 Widefield Imaging

To gather individual time series of the fluorescence signal of dozens of nanocrystals in parallel, widefield microscopy is used. This setup is illustrated in fig. 3.4. An alternative lens is used to realize widefield illumination of the sample as in the previous section and to project the sample's image onto a CCD camera (Andor Luca). It takes pictures of the quantum dot ensemble (an area of about 15 μm in diameter) at a rate of five frames per second and sends them to a computer software for recording (Andor Solis). Because of the much bigger illumination area on the sample, a higher excitation intensity is necessary, which is achieved with a continuous-beam argon ion laser (Coherent).
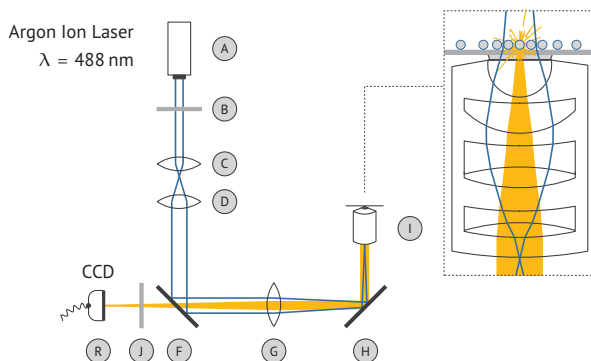
Fig. 3.4: Widefield microscope setup. Light from a continuous argon ion laser **(A)** is focused through a lens **(G)** into the back focal plane of the objective. A big area of the sample is excited, and its signal imaged onto the CCD camera **(R)** through the same lens (G).

3.2.5 Lifetime Measurements and Evaluation of Decay Histograms

The technique of single photon counting sketched in the previous sections allows the evaluation of the excited state lifetime of a fluorophore. The specific term is *Time Correlated Single Photon Counting* (TCSPC). It is based on measuring the delay time between a triggered excitation laser pulse and the arrival of the fluorescence response at the detector. These individual delay times τ are accumulated and can be assembled to a decay histogram (fig. 3.5). Since the delay distribution is caused by the exciton decay time, it can be used to evaluate the average excited state lifetime of the fluorophore (see section 2.2.4).

To measure the time-dependent (and therefore voltage-dependent) behavior of the average excited state lifetime during a CV cycle, decay histograms (fig. 3.5) are accumulated over a binning time of 4 s. The histograms usually show multi-exponential behavior, but the amount of noise does not allow for a stable fit of a bi-exponential function (eq. 2.34). Instead, a stable value for the short lifetime component is achieved by fitting a mono-exponential function to the very pronounced data at short times, as well as to the background y_0,

$$P_{\text{mono}}(\tau) = y_0 + A_{\text{short}} \exp\left(-\tau/\tau_{\text{short}}\right), \qquad \tau < 13 \, \text{ns} \ \text{ and } \ \tau > 210 \, \text{ns}. \qquad (3.3)$$

The result for τ_{short} is then kept constant while fitting a bi-exponential function to the complete datset:

$$P_{\text{bi}}(\tau) = y_0 + A_{\text{short}} \exp\left(-\tau/\tau_{\text{short}}\right) + A_{\text{long}} \exp\left(-\tau/\tau_{\text{long}}\right). \qquad (3.4)$$

Because there is less data available and no degree in freedom for τ_{short}, the result for the long component τ_{long} comes with a much higher relative error than the short component, but still gives meaningful values to discuss the qualitative behavior during CV cycles (see section 4.3.4).
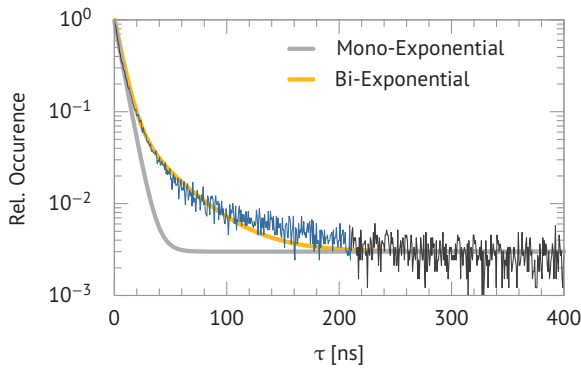

Fig. 3.5: Illustration of the fitting process for fluorescence decay histograms. A mono-exponential function (gray line) is used to fit to data at $\tau < 13$ ns and $\tau > 210$ ns for the short component. The parameter τ_{short} is then kept constant during a second fit of a bi-exponential function (yellow) to get an estimate of the long component τ_{long}.

3.3 ITO and ZnO/ITO substrates

The samples are top-mounted onto an oil-immersion objective during the measurements. This necessitates optically transparent sample substrates. Since the quantum dots must be adsorbed to a conductive electrode, this yields the use of semiconductor substrates. They are highly transmissive for optical wavelengths when they feature a big enough band gap.

For this work, glass substrates with ITO coatings (indium tin oxide) are used. ITO is an n-type semiconductor with a band gap of 2.9 eV, [73] but its optical band gap is even higher at ≈ 3.9 eV. [63] The ITO-coated glass substrates were manufactured by Diamond Coatings.

To investigate the influence of different semiconductor electrodes, an additional layer of ZnO is placed onto the ITO coating by Pulsed Laser Deposition at room temperature. [74] This coating procedure was kindly done by Holger Hochmuth in the PLD Lab of Prof. Lorenz in Prof. Grundmann's semiconductor physics group at the Universität Leipzig. Despite the fact that ZnO is a natural n-type semiconductor, [62] the effect of doping and therefore of a higher charge carrier density close to the conduction band was studied using ZnO coatings that exhibit a very high Ga_2O_3 doping of 0.1 % (atomic percent), referred to as Ga:ZnO in the following sections. Substrates with a ZnO layer thickness of 20 nm are used for the measurements presented in this work. The three substrates in use are illustrated in fig. 3.6.

(a) ITO on Glass   (b) ZnO/ITO   (c) Ga:ZnO/ITO
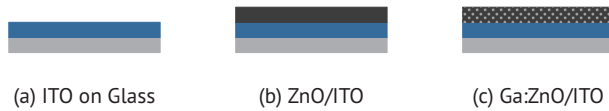
Fig. 3.6: The three substrates in use. **(a)** Indium tin oxide layers (ITO, blue) on glass (light gray) are used as a foundation for additional coatings of **(b)** pure ZnO (black) and **(c)** Ga_2O_3-doped ZnO films (black, dotted) of 20 nm thickness.

3.4 Sample Preparation

The quantum dots' fluorescence behavior will be observed on a transparent electrode. To ensure good electric contact, very dilute sub-monolayer concentrations of nanocrystals are placed on the sample substrate.

Before use, ITO is cleaned by rinsing the substrate with acetone, isopropanol, ethanol and purified water (Millipore Milli-Q) in that order, and then placed in a plasma cleaner for 20…30 min.

The ZnO/ITO and Ga:ZnO/ITO substrates are reused several times and therefore more thoroughly cleaned before use. They are rinsed with acetone, isopropanol, ethanol and purified water in that order. After being dried with nitrogen, they are put into a toluene bath at 65 °C and being subjected to ultrasonic cleaning. They are then transferred into spectroscopic grade ethanol solution, where they stay at 80 °C for 12…16 h, followed

by another hour in the ultrasonic cleaning bath at 65 °C (in previously refreshed spectroscopic ethanol). They are rinsed again with purified water, dried with nitrogen, and placed in a plasma cleaner for 20…30 min.

The original quantum dot solution is diluted to ≈ 200 nmol/l for ensemble measurements and ≈ 40 nmol/l for single quantum dot studies. They are spin cast onto the substrates at a rotation frequency of 4000 rpm.
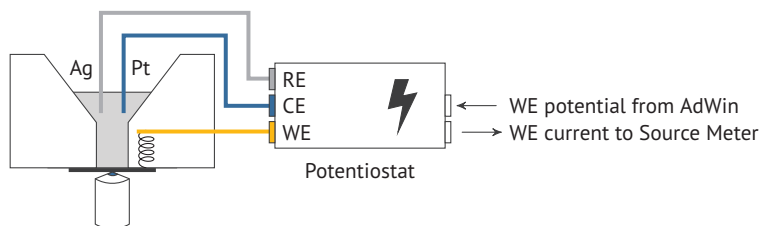
3.5 The Electrochemical Cell

To observe the nanocrystal fluorescence at tunable, well-defined and reproducible electric potentials, an electrochemical cell was built that is operated with a home-made potentiostat and can be mounted to the fluorescence microscope.

The setup is illustrated in fig. 3.7 and the individual parts for the electrochemical cell are shown in fig. 3.8. The sample substrate is placed on the microscope objective window of the sample holder and a teflon funnel is put on top. A copper spring is used to provide electric contact between the substrate which will serve as the working electrode and a connector that is driven into the funnel and will later be used to connect the working electrode (WE) to the electric circuitry from the outside. A teflon ring (hole-punched teflon disc) is placed between the sample and the funnel for additional sealing. The funnel is then pressed onto the substrate by tightening four screws that connect two steel plates which enclose the sample holder and the funnel. The silver wire quasi-reference electrode (RE) and the platinum wire counter electrode (CE) are placed on top of the funnel with regular tape.

The three-electrode setup is necessary to maintain a stable reference potential. As the potential of the working electrode is measured relative to a Ag wire quasi-reference, this reference must not change its own potential, i.e. it must be ensured that no currents due to repolarization flow between the reference electrode and the electrolyte solution. An electric device called the *potentiostat* takes on this task. It maintains the working electrode potential by directing all polarization currents through a third electrode, the counter electrode, and keeps the reference electrode current-free and therefore at a stable potential. The circuitry of the potentiostat is shown in fig. 3.9.

For the electrolyte solution, tetrabutylammonium perchlorate (TBAP) is solved in propylene carbonate (PC), at a concentration of c = 0.1 mol/l (before it dissolves into two ions, which leads to a molar ion concentration twice as high). For some measurements, the solution is dried using a molecular sieve with a pore size of 4 Å. Before use, the molsieve is dried at 200 °C under low air pressure (≈ 5 mbar) for at least 12 h.

The cell is in contact with air during all measurements. The wire electrodes are usually cleaned in H_2SO_4 solution (50 %) and then rinsed in acetone, isopropanol, ethanol and purified water.

Fig. 3.7: The electrochemical cell. A teflon funnel mounted on top of the sample substrate contains the propylene carbonate solution. Tetrabutylammonium perchlorate (TBAP) is the salt used to provide electrolyte ions. A three-electrode setup is employed with a reference electrode (RE, silver wire) and a counter electrode (CE, platinum wire). The sample is adsorbed to a flat, transparent semiconductor working electrode (WE) that is connected with a copper spring and wire. The potentiostat sets the desired potential of the working electrode relative to the Ag wire quasi-reference of constant potential.
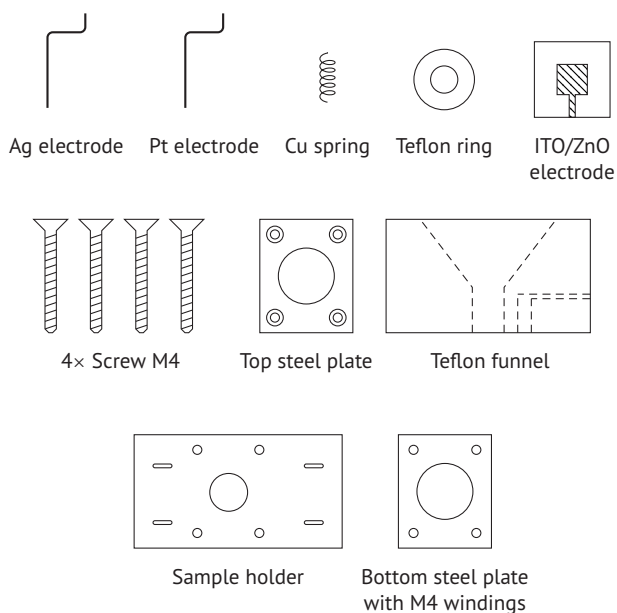
Fig. 3.8: Equipment used to assemble the electrochemical cell.
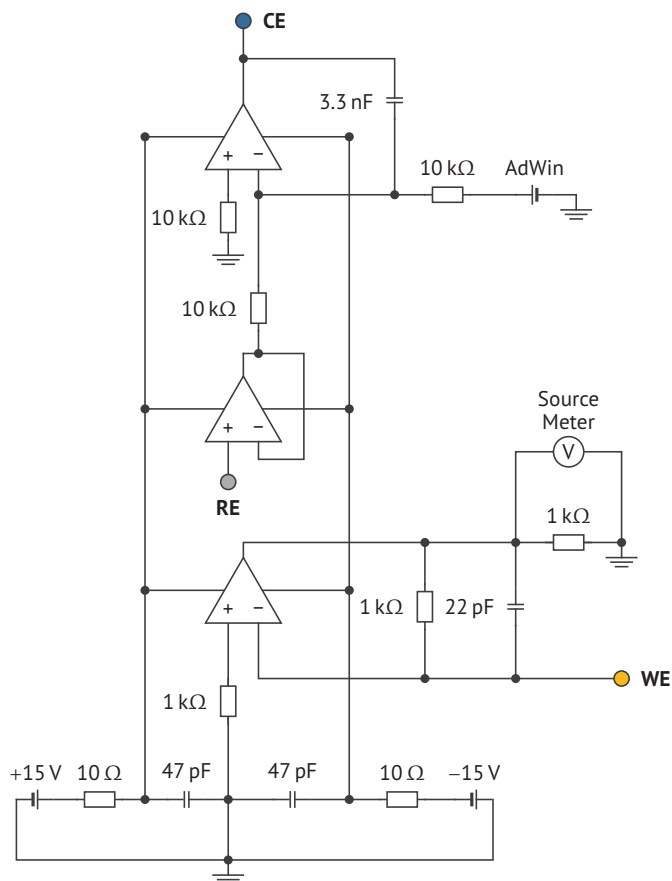
Fig. 3.9: Electric circuitry of the home-made potentiostat. For all three operational amplifiers, a model identical to the Texas Instruments TL081 is used. The Source Meter determines the electric current through the working electrode by measuring the voltage drop over a resistor. An AdWin Gold is used to enter the desired working electrode potential into the potentiostat circuitry. Both the Source Meter and the AdWin are connected to the computer software. The connectors for the working electrode (WE), reference electrode (RE) and counter electrode (CE) are labeled.

4 Experimental Results and Discussion

4.1 Influence of the Substrate

The quantum yield η and the excited state lifetime τ of the observed nanocrystals differ significantly with the substrate they are placed on and with the dielectric environment, i.e. whether they remain in air or are submerged in a solvent for electrochemistry, such as propylene carbonate. In addition to chemical properties and band alignment considerations, these factors play an important role in choosing suitable experimental conditions.

Figure 4.1 displays confocal microscopy scans of the same submonolayer ensemble concentrations of quantum dots on an ITO substrate as well as on a ZnO/ITO substrate. The overall intensity on the ITO substrate is about a factor of four higher than on the ZnO/ITO substrate.

(a) ITO   1 µm ▬   (b) ZnO/ITO   1 µm ▬
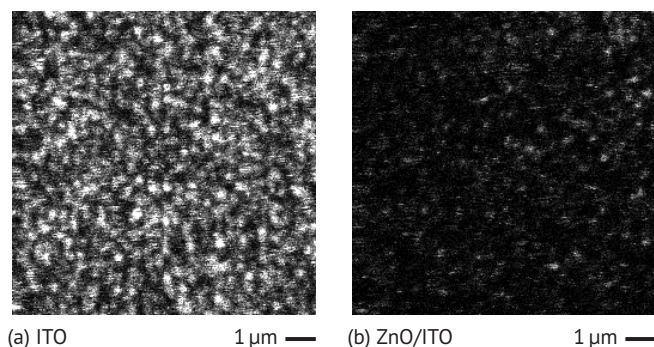
Fig. 4.1: Confocal microscopy scans of submonolayer quantum dot ensembles on an **(a)** ITO and a **(b)** ZnO/ITO substrate at excitation powers of 100 nW, both in air. Identical concentrations were used for the spin coats. The signal is normalized to the same value (25 000 counts/s, white) for both images.

The average excited state lifetime on ZnO/ITO is up to a factor of two lower than on pure ITO substrates (fig. 4.3a, b). To investigate the extent to which the proximity of a conducting surface contributes to the fluorescence quenching, ITO substrates are coated with polyvinyl alcohol (PVA) films of 2 nm, 15 nm and several 100 nm thickness before the quantum dot solutions are cast. For these layers, water solutions with a PVA mass concentration of 0.25 % and 1 % are produced and spin coated at 8000 rpm. The coated substrates are scratched with a knife and scanned with an atomic force microscope. The resulting height maps and height profile lines of interest are shown in figure 4.2a for the 0.25 % PVA solution and in figure 4.2b for the 1 % solution.

The applied scratches are clearly visible, whereas the height difference from the ripped PVA layer at the edges of the scratches are barely visible by eye. From the height profile measurements, the PVA layer thicknesses are estimated to be $d_{0.25\,\%} \approx 2\,\mathrm{nm}$ and $d_{1\,\%} \approx 15\,\mathrm{nm}$.
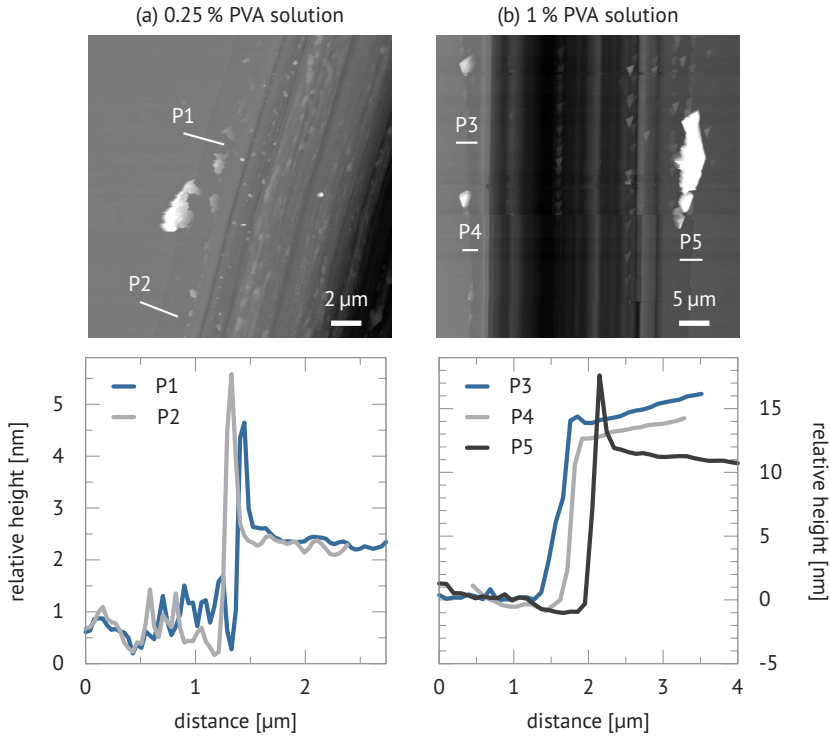
Fig. 4.2: Atomic force microscope measurements of PVA coated ITO substrates. Height profiles of interest are shown below each image. The PVA layers ripped at the edges of the clearly visible scratches that were applied prior to the measurement.

Excited state decays on all substrates are shown in fig. 4.3a. In fig. 4.3b they are related to the average intensity from the illuminated area, as captured in the wide field microscope mode.

Discussion

The decrease in intensity is accompanied by a proportional decrease in the excited state lifetime (fig. 4.3b), which means that more absorbed energy is transferred to nonradiative decay channels.

It is known that the luminescence of fluorescent particles is quenched in the proximity of semiconductor interfaces.[75] The nonradiative rate Γ_{nr} increases due to energy transfer from the particle to the semiconductor bulk. This increase can be expressed by an additional component in Γ_{nr}, namely the energy transfer rate Γ_{ET}. It has an inverse

cubic dependence on the distance d of the dipole to the surface:[76]

$$b_{\text{ET}} = \frac{\Gamma_{\text{ET}}}{\Gamma_{\text{r}}} = \frac{\theta \lambda^3}{4 (2\pi n_1 d)^3} \cdot \text{Im}\left(\frac{\epsilon_2 - \epsilon_1}{\epsilon_2 + \epsilon_1}\right),$$ (4.1)

where n_1 and ϵ_1 denote the refractive index and the dielectric constant of the medium around the particle, ϵ_2 the dielectric constant of the semiconductor bulk, λ the emission wavelength, and θ a dipole orientation factor (here $\theta \approx 1$).

Figure 4.3c shows the relative ensemble intensity in dependence on the distance of the quantum dot centers—where the dipole is expected to be—to the ITO substrate surface. Apart from the PVA layer, an additional distance of 4.8 nm is assumed as the nanocrystal radius measures about 2 nm and the surrounding ZnS shell and HDA ligand cover also have a total thickness of about 2.8 nm (see section 3.1).
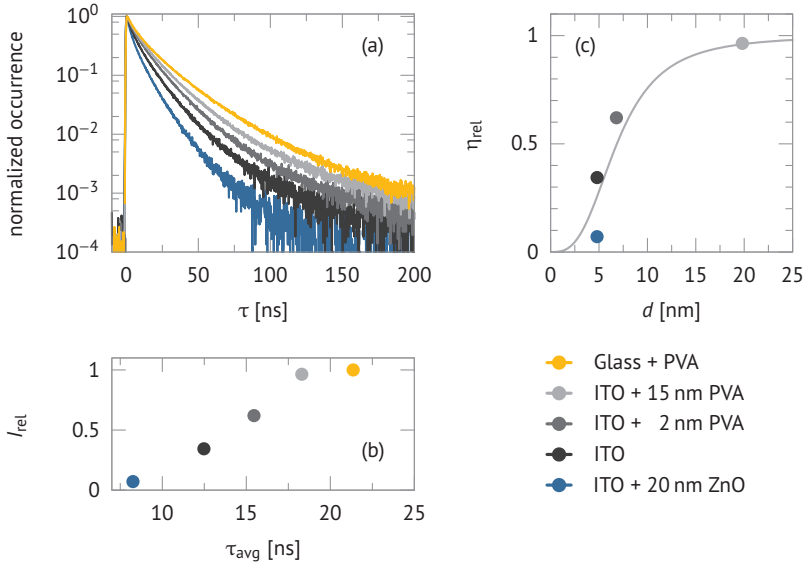
Fig. 4.3: (a) Excited state lifetimes of submonolayer ensembles of quantum dots in air on different substrates (glass, ITO, ZnO on ITO). ITO substrates are coated with layers of PVA to achieve various distances d between the nanocrystals and the substrate. Equal excitation powers of 50 nW were used. **(b)** Interdependence of relative intensity I_{rel} and excited state lifetime τ. The intensity on ZnO/ITO and ITO is normalized to one on ITO with a thick PVA layer of several 100 nm (not shown) where the lifetime τ is found to be as on a glass surface. This is done to account for the absorption of the ITO substrate. **(c)** Dependence of the relative intensity I_{rel} on the distance d of the nanocrystal centers to the surface. The relative quantum yield (eq. 4.2) is plotted for a substrate extinction coefficient $k = 0.01$, typical for ITO. Intensity normalization as in (b).

The intensity is normalized to the intensity far away from the ITO surface. For that purpose, a PVA layer of several 100 nm thickness is placed on an ITO substrate. Apart from the transmission losses due to ITO, the nanocrystal ensemble in that sample has the same intensity and lifetime as on glass and is used for the normalization factor as the ITO substrate influence is sufficiently small at high distances $d \to \infty$.

The relative intensity I_{rel} can now be treated like a relative quantum yield η_{rel} that would be expected if the overall nonradiative rate Γ_{nr} had no components other than the energy transfer rate Γ_{ET} to the semiconductor bulk:

$$I_{rel}(d) = \eta_{rel}(d) = \frac{\Gamma_r}{\Gamma_r + \Gamma_{ET}(d)} = \frac{1}{b_{ET}(d) + 1}. \tag{4.2}$$

This dependence is plotted in figure 4.3c for a substrate extinction coefficient $k = 0.01$ that is typical for ITO.[77] The peak emission wavelength of the quantum dot ensemble is at $\lambda = 601$ nm. The refractive index $n_1 = 1.53$ of PVA was used. The refractive index of HDA is sufficiently close ($n_{HDA} = 1.45$) and not expected to have significant impact on this approximation. A dielectric constant typical for ITO was chosen: $\epsilon_{2,ITO} = (2.1 + 0.01i)^2$.[77]

The relation between relative intensity I_{rel} and distance d (eq. 4.2) is shown to be in good agreement with the theoretical description for typical values of the materials used. However, the stronger luminescence quenching on ZnO cannot solely be explained by this model as its extinction coefficient k is usually equal to or even smaller than that of ITO[78] and should therefore result in a slightly higher relative quantum yield, not a lower one. This phenomenon will be further discussed in the following sections.

4.2 Absolute Electrode Potentials

As all voltages are measured relative to a silver quasi-reference electrode, its absolute electrode potential needs to be determined in order to draw conclusions from the change in the working electrode's and sample's Fermi level. To do so, the ferrocene/ferrocenium (Fc) redox couple with its well-studied redox potential is used as a reference system.[79, 80]

Ferrocene is dissolved in propylene carbonate (PC) to reach a concentration of $c = 5$ mmol/l and tetrabutylammonium perchlorate (TBAP, $c = 0.1$ mol/l) is added as an electrolyte. Cyclic voltammetry scans are performed for both anhydrous PC that was dried with molsieve (along with TBAP and ferrocene already in the solvent) for 3 days as well as for hydrous PC which was not treated. The scan rate for all experiments is 40 mV/s. Figure 4.4 shows the resulting voltammograms, i.e. the measured current I through the working electrode as dependent on the applied voltage. The working electrode in use is a platinum wire, whereas for the counter and reference electrodes a silver wire is used for each.

Measurements for different points in time are shown. $t = 0$ refers to the point in time when the measurements for the respective solvent are started; a few seconds after it was transferred into the electrochemical cell and started to be in contact with air. Each curve represents the third cycle of the respective measurement.

For the following fluorescence experiments substrates such as ITO, ZnO/ITO and Ga_2O_3-doped ZnO on ITO (referred to as Ga:ZnO/ITO) are used as working electrodes. Their performance upon reduction and oxidation of the Fc redox couple is shown for cyclic
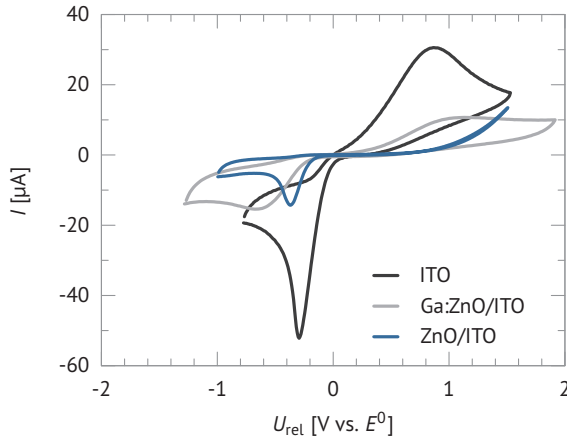
voltammetry scans in figure 4.5.
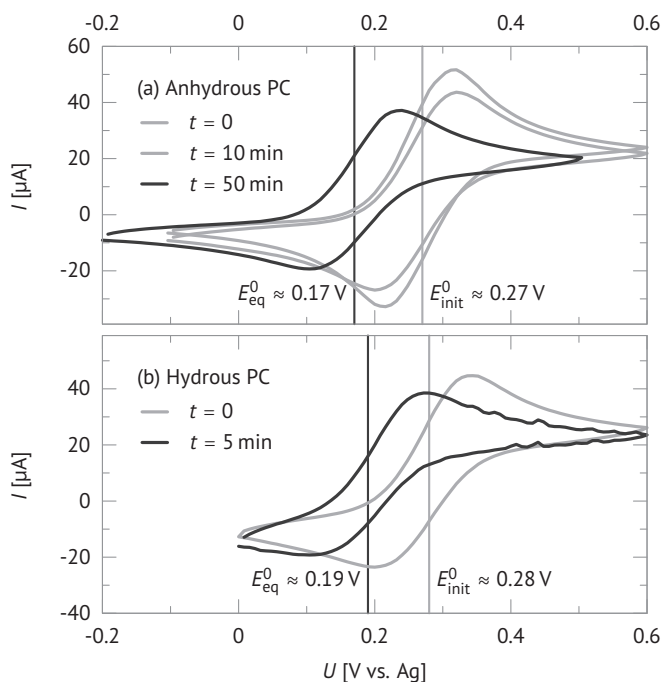
Fig. 4.4: Cyclic voltammetry of the ferrocene/ferrocenium redox couple (Fc, c = 5 mmol/l) solved in propylene carbonate (PC) with 0.1 mol/l TBAP as electrolyte. The current I through the Pt working electrode is measured in dependence of the applied potential U (relative to the silver wire quasi-reference) for both **(a)** anhydrous PC (treated with molsieve) and **(b)** hydrous PC. For the counter electrode a silver wire is used and a platinum wire for the working electrode. The scan rate amounts to 40 mV/s for all scans. The redox potentials E^0 are given for initial and equilibrium conditions.

Discussion

An Fc redox potential of $E^0_{eq} \approx 0.18$ V vs. Ag was measured for both hydrous and anhydrous propylene carbonate (PC). For hydrous PC (fig. 4.4b) this »equilibrium redox potential« is quickly reached within 5 min. Further CV cycles show no more shifting in the redox potential. For anhydrous PC (fig. 4.4a) it takes up to 50 min to reach this potential.

Both hydrous and anhydrous PC solution start off at a ferrocene redox potential that is about 0.1 V higher than the equilibrium potential: $E^0_{init} \approx 0.28$ V vs. Ag.

Using the Fc redox potential E^0_{eq}, the applied voltage against the Ag wire quasi-reference electrode can be converted to an absolute electrode potential that is measured against the energy of an electron in vacuum close to the solution interface, and can therefore be compared on a potential scale that is equivalent to the electron binding energy, common in solid state physics.[81] The established literature value for the Fc redox potential

Fig. 4.5: Cyclic voltammetry of the ferrocene/ferrocenium redox couple (Fc, c = 5 mmol/l) solved in propylene carbonate (PC) with 0.1 mol/l TBAP as electrolyte. ITO, Ga:ZnO/ITO and ZnO/ITO are used as working electrodes. Anhydrous PC (treated with molsieve) is used for all measurements. The curves are aligned such that U_{rel} = 0 V refers to the redox potential E^0 as determined separately for each experiment using a Pt wire working electrode to compensate for shifts in the potential of the Ag wire quasi-reference. The scan rate is 40 mV/s for ITO and ZnO/ITO, and 80 mV/s for Ga:ZnO/ITO.

compared to a standard hydrogen electrode is E_{Fc}^0 = 0.64 V vs. SHE.[82]. With the absolute electrode potential of the standard hydrogen electrode, E_{SHE}^0 = 4.44 V,[83] this leads to an absolute Fc redox potential of E_{Fc}^0 = (5.1 ± 0.1) V.[84] The three potential scales are shown in figure 4.6.
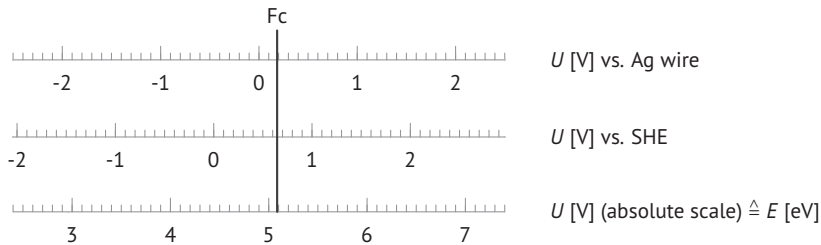
Fig. 4.6: Three potential scales of relevance. In the experiments, the voltage is measured against a silver wire quasi-reference electrode. Using the known ferrocene (Fc) redox potential, this can be converted to the scale of the standard hydrogen electrode (SHE) and to an absolute potential scale that refers to the energy of a free electron in vacuum, indicating the electron binding energy.

A comparison of ITO, Ga:ZnO/ITO and ZnO/ITO substrates as working electrodes (fig. 4.5) reveals that oxidation is inhibited for the all substrates, as seen from the oxidation peak's strong broadening and shift towards higher relative potentials compared to the symmetric behavior at a Pt wire working electrode (fig. 4.4).

On ZnO/ITO no oxidation peak is observed at all. This indicates that the band bending

at the surface (see section 2.3.2) does not allow any oxidation, i.e. electron injection into the substrate, at all within the scanned potential range. Frank and Bard[85] found similar behavior with an n-type TiO_2 electrode in acetonitrile solution when comparing a multitude of reactants of different redox potentials. Below the electrode's conduction band edge, reduction and especially oxidation were strongly inhibited.

On behalf of a clearer discussion, in the following sections **all voltages (in V) will describe the potential difference to the silver wire electrode,** whereas the absolute potential scale will be used to solely report energy levels (in eV). The affix *vs. Ag* will be dropped and is assumed to be the standard when reporting potentials.

4.3 Optically Detected Cyclic Voltammetry

4.3.1 General Measurement Scheme

To access a broad range of electrochemical potentials in the region of the nanocrystal conduction and valence bands, cyclic voltammetry (CV) scans are performed.

Submonolayer quantum dot ensembles are cast onto pure ITO, ZnO or Ga:ZnO/ITO substrates and placed in the electrochemical cell in hydrous propylene carbonate with 0.1 mol/l TBAP as electrolyte. Cyclic voltammetry scans with a scan rate of 10 mV/s are performed under wide-field illumination. The fluorescence photons from the illuminated ensemble are directed to an avalanche photo diode for time-tagged and time-resolved single photon counting.

Figure 4.7a shows a typical time series of the luminescence of an ensemble of nanocrystals at submonolayer concentration, collected in widefield mode (see section 3.2.4) as a triangular voltage sweep is applied.

At an applied potential of 0 V the fluorescence intensity starts at the same level that is also measured in equilibrium without any potential applied (the potentiostat being turned off). With decreasing potential, the intensity starts to rise until it reaches a peak value at about -1.6 V. From here, the signal begins to decrease until it reaches a low at -2 V where it is about a factor of two beneath the »equilibrium« intensity.

When the scan direction is reversed and the potential returns to higher values, a fluorescence peak is reached again, but neither the peak potential nor the peak intensity are reproduced. The peak is now broader, of less intensity and located at a significantly higher potential (-1.3 V).

Upon the return to 0 V the fluorescence intensity reaches its initial value again. A second cycle yields a slightly lower overall intensity, but the qualitative shape of the curve as well as peak positions are maintained as in the first cycle.
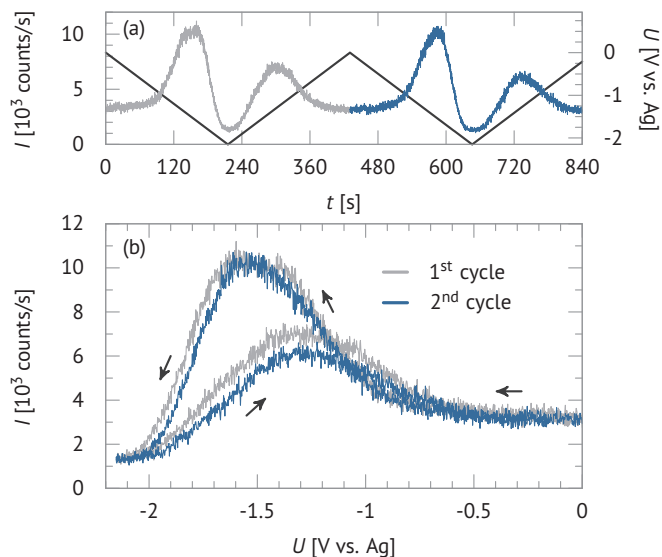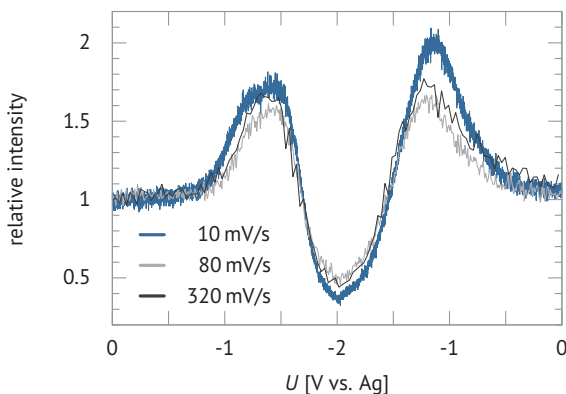
Fig. 4.7: Nanocrystal ensemble fluorescence intensity on Ga_2O_3-doped ZnO/ITO during cyclic voltammetry sweeps with a scan rate of 10 mV/s in hydrous propylene carbonate solution. **(a)** The voltage U between working and reference electrode is shown (black dashed line) as it is changed over time t. As a result, the fluorescence intensity I changes, displaying the same qualitative behavior during the first scan cycle (light gray curve) and the second one (blue curve). **(b)** The fluorescence voltammogram relates the registered intensity I to the applied voltage U. The scan direction is indicated by the arrows. First and second cycle are colored as in (a).

4.3.2 Scan Rate Independence

When cyclic voltammetry is used to investigate a sample in solution, the rate of oxidation and reduction is governed by the diffusion of the redox species because only molecules close[1] to the electrode will react. The behavior of the electric current through the working electrode is therefore dependent on the scan rate (see section 2.3.3). Even though a sample adsorbed to the working electrode does not underly diffusion, the rate of charge transfer may nevertheless be inhibited by potential barriers or poor electric conductivity. If such factors slow down the charge transfer rate to a value in the vicinity of the scan rate, they would also have an impact on a fluorescence voltammogram as seen in fig. 4.7. Therefore, the scan rate dependence is investigated.

Fluorescence voltammograms are taken on ZnO/ITO in hydrous propylene carbonate using triangular voltage sweeps at a scan rate of 10 mV/s, 80mV/s and 320 mV/s. Figure 4.8 shows the result. As the excitation power changes slightly during the experiment and individual quantum dots are known to bleach irreversibly, all intensities are normalized to the intensity of the respective curve at $U = 0$ V to maintain comparability of the scans.

---

[1] At a distance in the order of the Debye length.

Fig. 4.8: Fluorescence response to cyclic voltammetry scans of different scan rates. The sample is a submonolayer ensemble of nanocrystals on ZnO/ITO in hydrous propylene carbonate solution, measured in widefield mode. All intensities are normalized to the average intensity at 0 V to account for minor changes in the excitation power and bleaching of individual nanocrystals.

The different scan rates are chosen to span a range typical for the conducted experiments, from relatively slow (10 mV/s) to very fast (320 mV/s). They differ by a factor of 32, yet for the reduction scan (potential being lowered) the peak intensity, peak position, and overall fluorescence behavior remain unaffected (fig. 4.8). The same is observed for the peak position of the oxidation sweep. The height of the reverse peak should not be taken into account at this point. It is highly sensitive to the history of the previously conducted experiments and the time spent in very low potential regions (see section 4.3.5).

No dependence of the fluorescence response on the scan rate could be shown. The experiments are therefore not affected by any slow charge transfer rates between the substrate and the quantum dot ensemble.

4.3.3 Effect of Doping and Solvent Impurities

For the ZnO layer that is deposited on ITO substrates using Pulsed Laser Deposition, both pure ZnO and doped ZnO with 0.1 % Ga_2O_3 are used. The influence of the doping on the fluorescence behavior is investigated.

Fig. 4.9 compares the fluorescence response during reduction sweeps in both hydrous and anhydrous propylene carbonate on undoped and doped ZnO. Only the reduction sweeps are shown as the fluorescence during the oxidation sweep is highly sensitive to the time spent at very low potentials and the exact value of the return potential. This will be discussed in section 4.3.5.

The overall shape of the fluorescence trace does not qualitatively change with the doping, but for the doped substrate the fluorescence appears to be more enhanced at higher potentials $U > -1$ V compared to the pure ZnO layer. The potentials halfway between
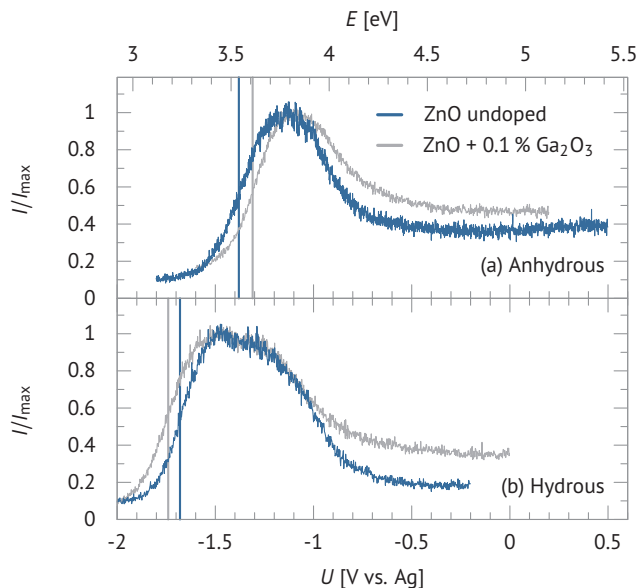
Fig. 4.9: Optically detected cyclic voltammetry with pure and doped ZnO layers deposited on ITO substrates. Only the reduction sweep (decreasing potential) is shown. The fluorescence response is displayed for **(a)** anhydrous and **(b)** hydrous propylene carbonate solution, the former one being treated with molsieve. The intensity I is normalized to each scan's respective intensity maximum I_{max}. The dashed lines indicate the potential positions U_0 halfway between fluorescence maximum and strongest quenching.

fluorescence maximum and strongest quenching (dashed lines in fig. 4.9) do not show any systematic shifts caused by the doping.

The presence of water and oxygen in the solvent not only alters the electrochemical potential at the working electrode (see section 4.2) but also causes an even stronger shift in the observed fluorescence behavior. Fig. 4.9 compares the result in hydrous and anhydrous propylene carbonate solution. The potential positions where the fluorescence drops halfway between maximum and strong quenching are shifted by $\Delta U \approx 0.4\,\text{V}$. The fluorescence peak under hydrous conditions is shifted and broader, and appears to consist of two components.

This shift cannot be explained by a shift in the potential of the reference electrode, as the redox potential of ferrocene only shows a maximum shift of about 0.1 V (fig. 4.4). The fluorescence of the nanocrystals is therefore highly sensitive to the amount of water and oxygen in the solvent. It has been shown that the density of states and band alignment of CdSe quantum dots changes strongly with the surface chemistry and dangling bonds. Hill and Whaley calculate the density of states for CdSe nanocrystals with saturated and unsaturated bonds on the surface.[86] For the unsaturated bonds, they find an altered electronic structure in both bands and a high concentration of states within the band gap, which causes the natural Fermi level (at 0 K) to rise by 1.5 eV. There is a high number of new states close to the conduction band. It is known that dangling bonds at the selenium sites react with oxygen in the environment to build SeO_2 and degrade

the crystal.[87] Furthermore, oxide semiconductors such as ZnO and ITO are known to show a high affinity to form bonds with hydroxyl groups or hydrogen,[88] which strongly alters the surface chemistry of the electrode.

4.3.4 Fluorescence and Lifetime Behavior on ITO and Ga:ZnO/ITO

The fluorescence behavior during cyclic voltammetry differs significantly with the substrate in use. Fig. 4.10a shows fluorescence voltammograms from ITO and Ga:ZnO.
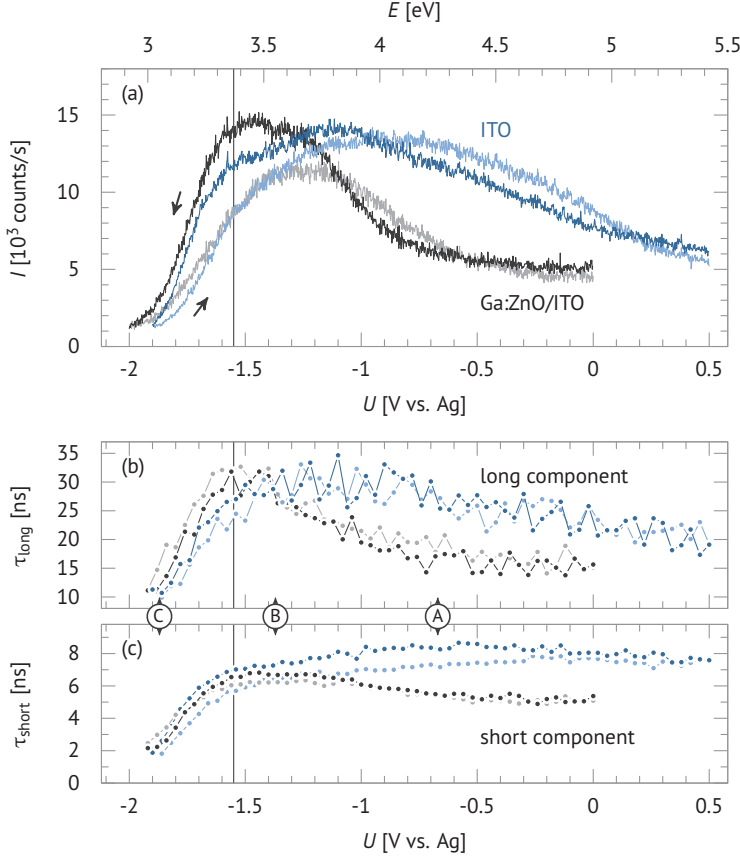
Fig. 4.10: (a) Optically detected cyclic voltammetry of submonolayer quantum dot ensembles on Ga:ZnO/ITO (black line) and pure ITO substrates (blue line). Both measurements are done in hydrous propylene carbonate. The lighter-colored lines indicate the corresponding oxidation scans upon return from the lower potentials. Both are scanned at 10 mV/s. The dashed line indicates the start of the potential region $U < -1.55$ V where the fluorescence decreases strongly during the reduction scan for both substrates. **(b)** Long and **(c)** short decay component of the excited state lifetime τ of the quantum dot ensembles. Each point represents the result of a bi-exponential fit to the lifetime histogram accumulated over a binning time of 4 s. Colors as in (a). For the positions A, B and C, the lifetime histograms are shown in fig. 4.11 along with the bi-exponential fit function.

On the ITO substrate, the quantum dots show strong fluorescence throughout a broad voltage range ($-1.5 \dots 0$ V, fig. 4.10a). During the reduction sweep, starting from 0.5 V, the signal slowly increases until it reaches a maximum at around $U_{max} \approx -1.1$ V where the intensity is twice as high as the initial one. From there, the signal decreases with the same slope at first. For very low voltages $U < -1.55$ V a very steep decrease in the fluorescence signal becomes apparent.

After about 50 s in this strongly quenching potential region, the oxidation sweep starts at -1.9 V. The fluorescence recovery is slower than the initial quenching and the behavior therefore not completely reversible. The maximum is reached at higher potentials at $U_{max} \approx -0.9$ V, around which the signal shape is almost symmetric throughout a broad potential region (± 0.5 V).

On the Ga:ZnO/ITO substrate, a stronger fluorescence quenching is visible at high potentials during the beginning of the reduction sweep. In a potential range from 0 V to about -0.8 V the signal stays at a level of ca. 50 % of the fluorescence maximum. When reaching lower potentials, a steep signal increase becomes apparent, which leads to a fluorescence maximum at -1.45 V. At even lower potentials $U < -1.55$ V, there is the same abrupt quenching behavior that is also observed in the ITO substrate.

The return behavior during the oxidation sweep is not reversible as well. The intensity maximum during this sweep is reached at a higher potential (at -1.25 V) and only reaches 75 % of the reduction sweep's maximum intensity.
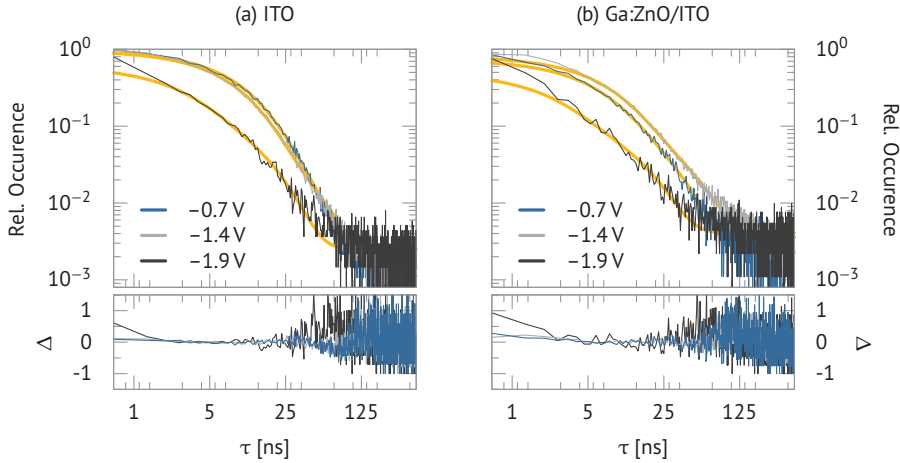
Fig. 4.11: Decay histograms for the excited state lifetime τ gathered over a bin time of 4 s at the potentials $U_A = -0.7$ V, $U_B = -1.4$ V and $U_C = -1.9$ V (see fig. 4.10) during the reduction sweep. The yellow lines in the background indicate the corresponding bi-exponential functions as the result of a two-step fitting process (section 3.2.5). The relative residual Δ is given in the two lower plots to show the deviation of the decay data from the fit function.

Both ITO and Ga:ZnO/ITO show qualitatively the same strong fluorescence quenching at potentials lower than -1.55 V. For a clearer picture of the underlying processes, the excited state lifetime is taken into account. Decay histograms (fig. 4.11) are accumulated

over a binning time of 4 s. A short-component lifetime τ_{short} and a long-component lifetime τ_{long} and their respective weights are gained by fitting a bi-exponential function to the data, a two-step process described in section 3.2.5. The two components are plotted in fig. 4.10b,c. The fit functions and relative residuals Δ are displayed in fig. 4.11 and show the deviation of the histogram data D from the fit function $P(\tau)$:

$$\Delta = \frac{D(\tau) - P(\tau)}{P(\tau)}. \tag{4.3}$$

The residuals show the rise of an additional, long component around $\tau = 60$ ns on ITO at a very low potential of $U_C = -1.9$ V. At this point, the deviation from the fit function rises to about $+100\,\%$, which is not seen at the other two potentials A and B, and can also not be discerned on the Ga:ZnO/ITO substrate. However, the magnitude of the deviation is of the order of the experimental error. Much longer integration times would be necessary to quantify this additional long component, and it is obvious that it does not significantly contribute to the overall fluorescence behavior.

Long Component Behavior

From figure 4.10 it becomes apparent that the overall behavior of the long-component lifetime τ_{long} follows the fluorescence behavior of the reduction sweep very closely on both substrates. It shows reversibility during the oxidation sweep within the error and therefore doesn't match the delays which are seen in the intensity when returning to higher potentials. Fig. 4.12a and c show the correlation between the lifetime τ and the fluorescence intensity I for the long component. For the reduction sweep, this correlation is linear and the two phenomena are therefore assumed to be linked. Since the lifetime τ and the quantum yield η, which is proportional to the intensity I, are proportional to each other,

$$\tau = \frac{\Gamma_r}{\Gamma_r + \Gamma_{nr}} \quad \propto \quad \eta = \frac{1}{\Gamma_r + \Gamma_{nr}}, \tag{4.4}$$

this means that for this component the radiative rate Γ_r stays constant during the reduction sweep and a change in the nonradiative rates Γ_{nr} may cause the intensity differences. On ITO, the correlation during the oxidation sweep is mostly linear as well, whereas on Ga:ZnO/ITO, the discrepancy between the highly reversible lifetime behavior of the long component and the delayed return of the fluorescence signal becomes visible.

Using equation 2.35 to calculate the absolute contribution to the fluorescence intensity reveals that the signal from the long component on **ITO** is relatively low and only increases slightly from around 12 % to 20 % of the fluorescence maximum throughout the reduction sweep, as shown in fig. 4.13a. The oxidation behavior is reversible. Only at very low potentials $U < -1.8$ V the long component's contribution vanishes almost instantly during the reduction cycle and returns at a lower rate upon sweep reversal.

This mainly low and constant contribution means that the long component has only minor influence on the fluorescence behavior and especially not on its shape. The change
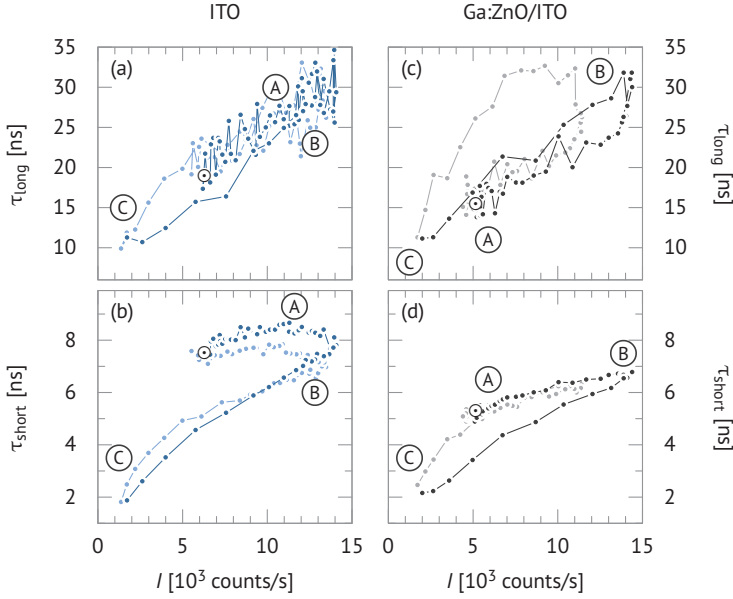
Fig. 4.12: Short **(a, c)** and long **(b, d)** decay component of the excited state lifetime τ related to the fluorescence intensity I on the two different substrates ITO and Ga:ZnO/ITO during the CV cycle displayed in fig. 4.10. The potential positions A, B and C and the meaning of the line colors are the same. The start and finish of the cycle is marked by ⊙.

in τ_{long} is solely responsible for the slight rise in the contribution C_{long}, the weight A_{long} stays constant. This can be interpreted by a fixed number of quantum dots in this »long component state« population, or the transfer rates into and out of this population are equal and not influenced by the electric potential of the substrate. However, the nonradiative rate Γ_{nr} does respond to the voltage.

There is a different picture on **Ga:ZnO/ITO** (fig. 4.13b). Here, the long and short components' contribution both qualitatively follow the fluorescence behavior seen in fig. 4.10a in the reduction sweep as well as in the oxidation sweep. Their maxima are slightly shifted around the fluorescence maxima at $U_{max,1} = -1.45\,\mathrm{V}$ (reduction sweep) and $U_{max,2} = -1.25\,\mathrm{V}$ (oxidation sweep). As the short component also mostly behaves directly proportional to the intensity (fig. 4.12d), this indicates that there are no two distinct subsets of quantum dots on Ga:ZnO/ITO, but a rather broad distribution of decay rates.

Short Component Behavior

After it has been found that two distinct components cannot be discerned on Ga:ZnO/ITO, and the long component population has no influence on the shape of the fluorescence signal on ITO, the behavior and impact of the short decay component on the **ITO** substrate remains to be discussed.
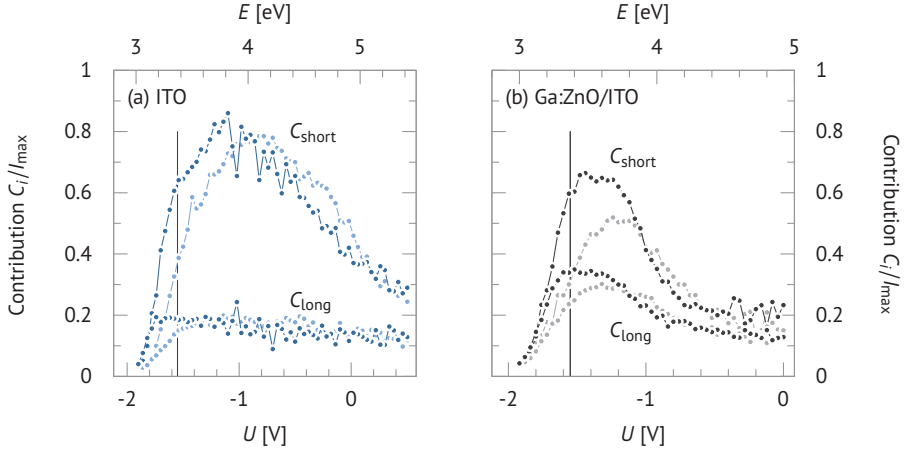
Fig. 4.13: Absolute contribution $C_i = A_i\tau_i$ of short and long decays to the fluorescence intensity. The contribution is normalized to the overall fluorescence maximum I_{max} of the **(a)** ITO and **(b)** Ga:ZnO/ITO substrate, respectively. The dotted line at $U = -1.55\,$V is the same visual guide as found in fig. 4.10 to indicate the potential of the sudden fluorescence drop.

The short component's decay lifetime stays constant at a value of about $\tau \approx (8 \pm 1)\,$ns throughout a very broad voltage range $U = 0.5\ldots -1.2\,$V during the reduction cycle, until the fluorescence reaches its maximum at a value twice as high as the initial intensity at the start of the cycle (fig. 4.10c and fig. 4.12b). The rise in the fluorescence signal is therefore attributed either to **(I)** a rise of the population number, i.e. previously completely dark quantum dots join the short-lifetime population and contribute to the fluorescence, or **(II)** the radiative rate Γ_r of the quantum dots increases in the same amount as the nonradiative rate Γ_{nr} decreases, which would yield a constant lifetime τ_{short} but an increase in the fluorescence signal. A combination of both is possible as well.

Past the fluorescence maximum, in the strong quenching regime at very low potentials, the correlation between the lifetime τ_{short} and the fluorescence intensity is mostly linear (fig. 4.12b). The lifetime drops to 25 % of its value at the intensity maximum, whereas the contribution C_{short} drops to less than 10 % (fig. 4.13a). This means that the fluorescence quenching can be explained by both a strong increase in the nonradiative rate Γ_{nr}, and a decrease in the weight A_{short}, which drops to about 40 % of its maximum value. Many quantum dots can be considered completely dark in this regime.

Upon reversal of the voltage slope at the beginning of the oxidation sweep, the recovery of the lifetime τ_{short} is delayed compared to the quenching (fig. 4.10c and fig. 4.13a), but slightly faster than the intensity recovery. It stays slightly below the values from the reduction sweep until relatively high potentials of $U > -0.3\,$V, where they match again.

Band Alignment

For an explanation of the underlying processes, the band alignment of both the electrode materials and the quantum dots needs to be considered. Fig. 4.14 shows an energy band diagram and the potentials of interest $U_A = -0.7\,\text{V}$, $U_B = -1.4\,\text{V}$ and $U_C = -1.9\,\text{V}$ (see fig. 4.10). Walsh *et al.* determined that the band gap of ITO has an upper limit of 2.9 eV.[73] The substrates used in this work are treated with oxygen plasma for about 1 h before they come to use—a process that is known to alter the surface chemistry and band alignment of the material. Christou *et al.* report a value of 4.69 eV for the work function of ITO after such treatment,[89] and Kuo *et al.* determined a value of 4.21 eV for ZnO films.[90]

In a study by Kaspar *et al.*, both ZnO as well as Ga:ZnO films deposited on ITO show no band bending at the material interface, but rather type II band alignment with a Ga:ZnO to ITO offset of −0.6 eV after 60 min exposure to oxygen plasma.[91] The doping did not have any significant influence. The Ga:ZnO-ITO heterojunction shows ohmic behavior,[92, 93] which is verified experimentally by a linear current-voltage dependence with the Ga:ZnO/ITO substrates used in this work.

The valence and conduction band energies of CdSe nanocrystals have been studied by Jasieniak, Califano and Watkins using photoelectron spectroscopy.[94] For nanocrystals with their first absorption peak at 2.1 eV, as used in this work (fig. 2.5), they found approximately $E_{\text{CBM}} \approx 3.3\,\text{eV}$ and $E_{\text{VBM}} \approx 5.4\,\text{eV}$.

ZnS features a much higher band gap than CdSe and forms a type I heterojunction with the nanocrystal core. For the ZnS-CdSe valence band offset, a value of $\Delta E_v = -0.6\,\text{eV}$ has been calculated by Wei and Zunger.[95] The shell has a thickness of at most two atomic monolayers and may act as a charge barrier. Due to its high surface area, many mid-gap trap states as a result of dangling bonds are to be expected.

Interpretation

The onset of the fluorescence increase on the Ga:ZnO/ITO substrate at potential position $U_A = -0.7\,\text{V}$ coincides with the substrate's Fermi level reaching its conduction band (fig. 4.14), which is now being occupied by electrons. Before this point, at higher potentials, the fluorescence is quenched and stays at a rather constant level. Both lifetime components are short for potentials higher than U_A, and rise along with the fluorescence once this potential is passed.

The behavior on ITO is different: even at high potentials, the fluorescence is already stronger than on Ga:ZnO, and rises over a broad potential range between $U = 0.5\,\text{V} \ldots -1\,\text{V}$. In this range, the short lifetime component stays constant and is higher than on Ga:ZnO. This hints at an additional quenching process on Ga:ZnO at higher potentials, as opposed to ITO. Since the substrate's conduction band is not filled with electrons at these mid-gap potentials, it mostly represents the situation when no voltage is applied. The short lifetime and weak fluorescence of nanocrystals on ZnO in air (fig. 4.3) is therefore likely the result of the additional quenching process seen here.
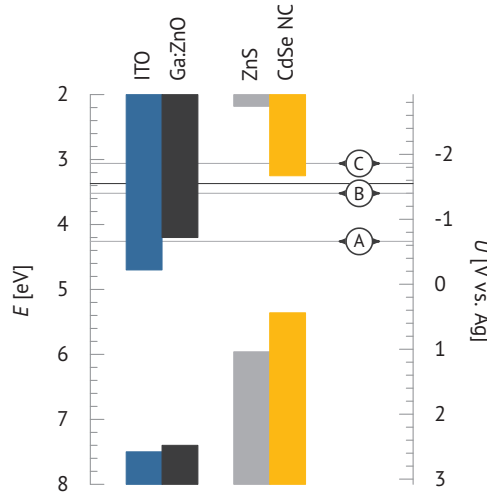
Fig. 4.14: Energy band diagram of the materials involved (see text for values and references). The dashed line indicates the beginning of the strong quenching regime at $U = -1.55$ V and A, B and C label potential positions of interest as in fig. 4.10.

The abrupt quenching at potentials $U < -1.55$ V (fig. 4.10a, dashed line) is a common trait of the fluorescence on ITO and Ga:ZnO/ITO. Here, the Fermi level of the substrate reaches the conduction band of the CdSe nanocrystal core. Many publications report the same quenching behavior [76, 96, 97] that is commonly interpreted by electron injection into the nanocrystal conduction band, which causes strong Auger quenching [98, 18] (see fig. 2.7d). The rising component in the decay histograms (fig. 4.11) at very short lifetimes $\tau < 2$ ns for the low potential $U_C = -1.9$ V on both substrates can very confidently be attributed to Auger quenching due to negative trions. Qin and Guyot-Sionnest found lifetimes for the negative trion between 0.5 ns (for 3 nm crystal diameter) and 0.9 ns (5 nm diameter) at CdSe/CdS quantum dots, [17] and an even shorter value of 0.15 ns for CdSe/ZnS crystals (5 nm diameter). [96]

4.3.5 Influence of the Reversal Potentials

The voltammograms pictured in the preceding sections indicate that the lower reversal potential plays a decisive role for the dynamics of the fluorescence recovery upon return from the strongly quenching potential region. A systematic approach to investigate this dependence is taken in this section.

Optically detected cyclic voltammetry is done on a Ga:ZnO/ITO substrate in anhydrous propylene carbonate solution. The lower reversal potential is systematically driven to more negative values, starting from $U_{low} = -1.3$ V down to -2 V in steps of -0.1 V. The upper reversal potential is kept constant at $U_{high} = +0.2$ V. The time traces of the fluorescence signal and the applied voltage are shown in fig. 4.15a.
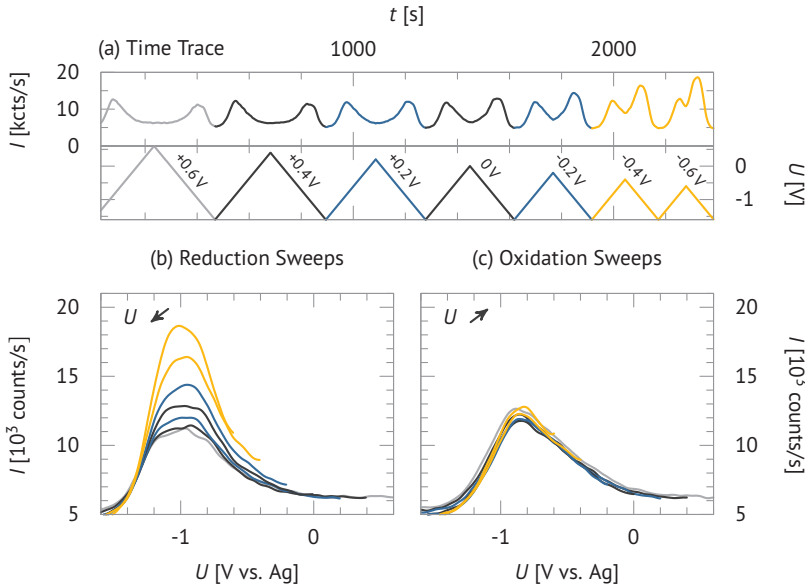
The signal during the oxidation sweeps upon return from the different lower rever-
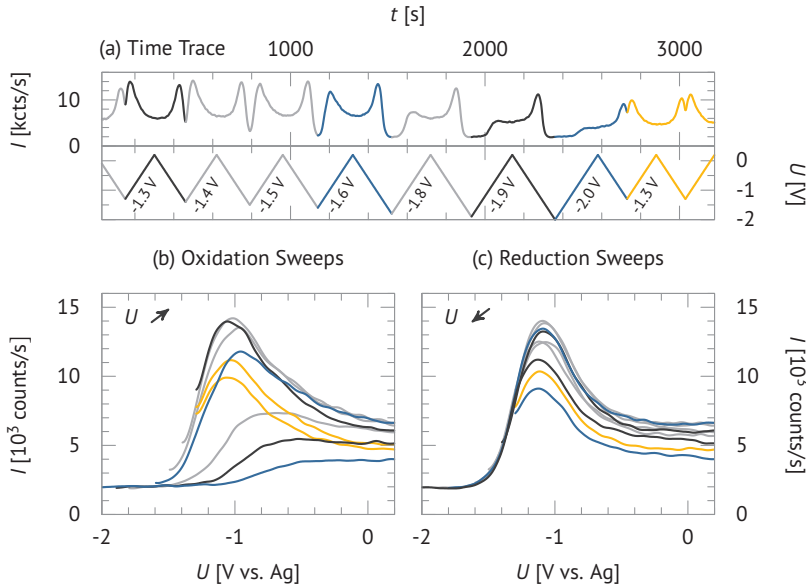
Fig. 4.15: Optically detected cyclic voltammetry sweeps on Ga:ZnO/ITO substrate with a systematic change of the lower reversal potential. The upper reversal potential is kept constant at a value of U_{high} = +0.2 V. In **(a)** the time trace of the fluorescence signal (upper graph) and the applied voltage (lower) are shown. The numbers in the voltage time trace give the value of the reversal potential. The colors in the voltammograms of **(b)** the oxidation sweep and **(c)** the reduction sweep are the same as in (a). The fluorescence curves have been smoothed for clarity.

sal potentials is shown in fig. 4.15b. With increasingly negative reversal potentials, the peak's position shifts noticeably towards higher potentials and it decreases in height. Until U_{low} = −1.8 V, the fluorescence fully recovers when reaching the upper reversal potential at U_{high} = 0.2 V. For these, the overall shape and peak height during the subsequent reduction sweep (fig. 4.15c) is the same. However, for the even lower reversal potentials at U_{low} = −1.9 V and −2 V, the fluorescence does not fully recover and does not reach the original peak height during the subsequent reduction sweep (black and blue dashed traces in figs. 4.15b and c). During another two cycles to the initial reversal potential U_{low} = −1.3 V (yellow traces) the fluorescence still does not fully recover to its original intensity from the beginning of the experiment. However, the peak position during the oxidation sweep already reaches the peak potential U_{peak} = −1.1 V from the initial scans.

The delayed fluorescence recovery is not a result of slow charge transfer rates between the working electrode and the nanocrystals, as seen in section 4.3.2. The shift of the fluorescence peak position during oxidation sweeps towards higher potentials (fig. 4.15b) means that the fluorescence recovery from very low potentials takes place on a time scale that is of the same order of magnitude as the cycle time. The conditions at the high reverse potential U_{high} = +0.2 V only seem partly suited to undo the effects of the strong quenching regime. Whereas the peak position during the subsequent reduction

Fig. 4.16: Optically detected cyclic voltammetry sweeps on Ga:ZnO/ITO substrate with a systematic change of the upper reversal potential. The lower reversal potential is kept constant at a value of $U_{low} = -1.6$ V. In **(a)** the time trace of the fluorescence signal (upper graph) and the applied voltage (lower) are shown. The numbers in the voltage time trace give the value of the reversal potential. The colors in the voltammograms of **(b)** the reduction sweep and **(c)** the oxidation sweep are the same as in (a). The fluorescence curves have been smoothed for clarity.

sweep is the same, the intensity does not fully recover (fig. 4.15c). This may hint at two subsets of fluorescence states induced at very low potentials: very long-lived dark states that do not contribute to a shift in peak positions, but are not significantly »healed« at the high reversal potential, and more short-lived dark states, or states with altered blinking dynamics, that recover on a time scale observable during the oxidation sweep, which leads to a shift in the intensity peak. The latter quenched states may be undone at higher potentials and cause no shift in the peak position during the subsequent reduction sweep.

The recovery is also investigated in dependence on the upper reversal potential U_{high} (fig. 4.16). As U_{high} is systematically decreased in steps of -0.2 V from $U_{high} = +0.6$ V to -0.6 V, the fluorescence peak remains at the same position at $U_{peak} = -1.1$ V, but increases significantly in intensity.

The recovery from the strong quenching region at very low potentials is highly reproducible for all oxidation sweeps (fig. 4.16c). High potentials seem to lead to very long-lived dark states that are undone when electrons are injected into the nanocrystal conduction band. The fluorescence peak intensity during the subsequent reduction sweep increases as very strong return potentials U_{high} are more and more avoided. Electron ejection at high potentials and subsequent surface oxidation are commonly associated with strong quantum dot off states.[17] The measurements presented here suggest that

		U_0 [V]	σ [meV]	FWHM [meV]
Anhydrous	ZnO	−1.40(3)	126(15)	298(35)
	Ga:ZnO	−1.32(2)	102(2)	240(5)
Hydrous	ITO	−1.67(1)	96(10)	226(24)
	ZnO	−1.69(2)	96(4)	226(9)
	Ga:ZnO	−1.74(1)	110(3)	259(7)

Tab. 4.1: Mid-quenching potential U_0 halfway between fluorescence maximum and strong quenching region during reduction sweeps. The width σ of the assumed Gaussian injection edge distribution is given. All errors are standard deviations from several results per material. The full width at half maximum (FWHM) is given as well.

recovery from these states is possible when electrons are injected back into the crystals.

In both experiments the onset of the strong quenching at low potentials and the position of the electron injection edge are not dependent on the positions of the reversal potentials $U_{\min}$ and $U_{\max}$. The general method is therefore suited to determine the location of the conduction band.

4.3.6 Distribution of Injection Edges

For the case of a Gaussian distribution of the conduction band edges of the nanocrystals, its width σ can be determined from the fluorescence behavior at the very low, strongly quenching potentials during reduction sweeps. Assuming that electron injection into the conduction band immediately turns a quantum dot dark whereas it has been in a bright state before, the intensity I at potential U is the integral over the part of the Gaussian distribution of nanocrystals that are still »on«:

$$I(U) = \frac{I_{\max} - I_0}{\sqrt{2\pi}\sigma} \int_{-\infty}^{U} \exp\left(-\frac{(u - U_0)^2}{2\sigma^2}\right) du + I_0, \tag{4.5}$$

where I_0 denotes the constant background intensity and U_0 the potential where half of the nanocrystals are in the »dark« state. $I_{\max}$ is the maximum intensity (where all quantum dots are assumed »on«). There is no elementary solution for the integral in the cumulative distribution function in equation 4.5. It can be expressed in terms of the error function:

$$I(U) = \frac{I_{\max} - I_0}{2}\left[1 + \mathrm{erf}\left(\frac{U - U_0}{\sqrt{2}\sigma}\right)\right] + I_0. \tag{4.6}$$

The values of the error function can easily be calculated numerically.

The mean injection edge potential U_0 and distribution widths are listed in table 4.1 as the average result from several fits under the given conditions. The effect of solvent impurities in hydrous propylene carbonate on the injection potential is evident, as already discussed in section 4.3.3. No systematic dependence of the distribution width on the substrate or solvent impurities is apparent.

The size dispersion of the nanocrystals leads to a distribution of exciton energies due

to stronger or weaker confinement and therefore to a distribution of conduction band minima. The peak width in fluorescence spectra (fig. 2.5) is mostly governed by the ensemble's size dispersion and can therefore serve as an upper limit to the effect it can have on the distribution of the injection edges. The full width at half maximum of the spectra seen from quantum dots in toluene is in the region of FWHM $= (135 \pm 5)$ meV. This number refers to the distribution of band gap energies and contains contributions from both valence and conduction band offsets. It can therefore not fully account for the broader distribution seen here.

The assumption of two strictly distinct »on« and »off« states when lowering the potential seems wrong. A scenario with competing electron injection and ejection rates k_{in} and k_{out} is more likely and could cause a change in the blinking dynamics of the nanocrystals throughout a specific potential range. Jha and Guyot-Sionnest found a similarly broadened quenching distribution and observed modified blinking statistics when measuring the response of single CdSe/CdS quantum dots to switches in the electrochemical potential. [76]
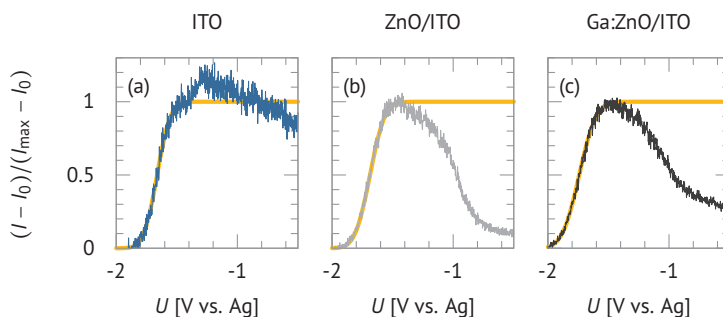
Fig. 4.17: Fluorescence signal during reduction sweeps on **(a)** ITO (blue), **(b)** ZnO/ITO (gray) and **(c)** Ga:ZnO/ITO (black) substrates under hydrous conditions. The yellow lines in the background show the result of a fit to the data for strong quenching potentials using equation 4.6. The intensity *I* is normalized to the maximum intensity I_{max} assumed from the fit, and the background I_0 is subtracted.

Figures 4.17a, b, and c show fits of the function in equation 4.6 to the fluorescence response at low potentials. The data is normalized to the maximum intensity I_{max} assumed from the model, and the background I_0 is subtracted. For ZnO and Ga:ZnO/ITO, a purely Gaussian distribution of quenching potentials matches the data. For ITO, however, an additional fluorescence component is visible. Its quenching process seems to take place +0.13 V before the strong quenching mechanism that is seen on all substrates. This component is completely missing on both ZnO/ITO substrates, as also seen in the previous section 4.3.4, which is a trait characteristic to ZnO/ITO, both doped and undoped, and shows the strong impact of the substrate choice. The cause may be a difference in the nature of the interaction between the substrate and the quantum dot surface and its trap states. The origin of this effect must be the subject of further studies.

4.3.7 Single Nanocrystals

For a deeper understanding of the ensemble's fluorescence dynamics, each nanocrystal's individual contribution to the overall signal should be taken into account. In this section, widefield imaging is used to establish an approach to investigate the fluorescence traces of single quantum dots.

A sub-ensemble concentration of nanocrystals on Ga:ZnO/ITO substrate in anhydrous propylene carbonate solution is observed using the setup explained in section 3.2.4. A total of 6000 CCD frames is collected while scanning eight consecutive CV cycles with reversal potentials U_{high} = 0 V and U_{low} = −1.6 V at a scan rate of 20 mV/s. The time between two frames is 200 ms.

An average of these 6000 frames is shown in fig. 4.18a. The relatively strong background intensity makes it difficult to discern single nanocrystals. Therefore, their blinking nature is used as a property that sets them apart from the rather constant background intensity. A map of each pixel's time trace variance $\sigma^2 = \langle I^2 \rangle - \langle I \rangle^2$ is calculated (fig. 4.18b) and used to identify single quantum dots by finding the local maxima.

(a) Image Average   2 µm ▬   (b) Variance Map   2 µm ▬
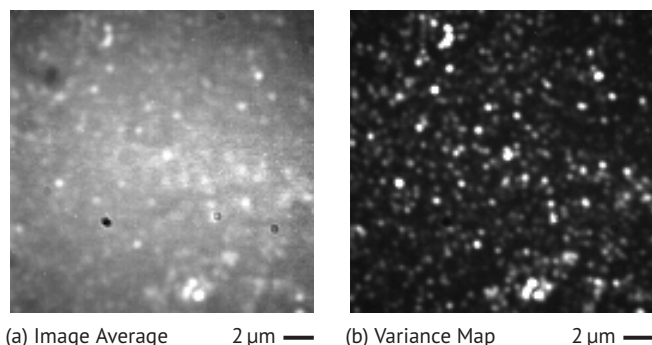
Fig. 4.18: (a) Average widefield image accumulated from 6000 camera frames that were recorded during eight consecutive CV cycles with reversal potentials U_{high} = 0 V and U_{low} = −1.6 V. **(b)** Map of the variance of each pixel's intensity throughout the 6000 frames accumulated during the CV cycles mentioned for (a). Higher variation is indicated by lighter gray values.

174 nanocrystals are identified by this method. The fluorescence during an average CV cycle—accumulated over all eight consecutive cycles—is shown as a gray value map in fig. 4.19a. Each horizontal line represents the average time trace of one quantum dot. An attempt has been made to fit the cumulative distribution function from equation 4.6 to the average CV cycle trace of each quantum dot in the strongly quenching potential region. This is not satisfyingly possible for all nanocrystals because of the blinking behavior and the limited amount of CV cycles that contribute to the average. Nevertheless, the traces in fig. 4.19a are ordered by their average »turn off« potential U_0 as a result from the fit. A more meaningful sorting method is still to be found. However, it becomes apparent that there is a broad distribution of »turn-off« potentials. In figs. 4.19b and c, four selected CV traces are shown for the nanocrystals #24 and #99, respectively. There is usually a potential below which no further fluorescence is detected (dashed lines). This potential vastly differs from crystal to crystal, and has

been found in a range from −0.8 V to −1.5 V. Before that point, they show the typical fluorescence blinking. Around the upper reversal potential U_{high} = 0 V most quantum dots still show fluorescence. It is usually dominated by more or longer »off« states. In some cases, complete fluorescence quenching is observed, but it is clear that surface oxidation and subsequent complete fluorescence quenching does not yet play a decisive role in this potential region.
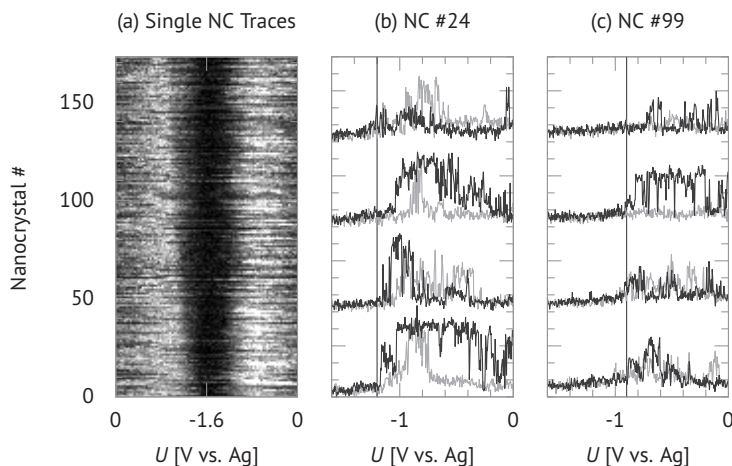
Fig. 4.19: (a) Single nanocrystal time traces averaged over eight consecutive CV cycles. Higher fluorescence intensity is represented by lighter gray values. Each horizontal line represents one quantum dot. The left side of the map shows the reduction sweep from 0 V to −1.6 V, the right side the oxidation sweep back to 0 V. The traces are sorted by their mean injection edge potential U_0 from a fit using eq. 4.6. In **(b)** and **(c)** four individual CV traces are shown for two specific quantum dots. Black traces show the fluorescence response during reduction sweeps, gray traces the oxidation sweep. The dashed lines indicate the threshold potential where each quantum dot is always »off« for lower potential values.

The CCD frame time of 200 ms does not allow the detection of high-frequency blinking, but the evaluation of widefield traces is still a promising tool to further investigate the nature of the underlying processes. Detecting the fluorescence signal of single nanocrystals using confocal microscopy would allow an even deeper insight, as the much better time resolution permits a detailed blinking and lifetime analysis. Unfortunately, no representative results could be gained within the time frame of this work.

From the widefield data presented here it becomes clear that the composition of the ensemble fluorescence traces is complex and involves many processes that have an impact on the luminescence of a single dot. Nevertheless, the high reproducibility of the ensemble traces still implies that the fluorescence is governed by distinct processes and mechanisms attributable to certain potential regions.

5 Conclusions and Outlook

The work presented here illustrates a way to combine conventional cyclic voltammetry with the simultaneous measurement of the luminescence signal from an adsorbed species at the working electrode. This technique allows a detailed investigation of the processes that affect the fluorescence in different oxidation states of the adsorbed fluorophore. For this work, the method was used to specifically investigate CdSe/ZnS nanocrystals and the effects that electron injection and ejection at different potentials have on the behavior of the ensemble and single crystal fluorescence. In addition, the impact of the substrate choice and its interplay with enhancement and quenching processes became apparent.

From conventional cyclic voltammetry measurements of the ferrocene/ferrocenium redox couple it became clear that oxidation processes, i.e. electron injection into the electrode, are inhibited for all substrates used—especially for undoped ZnO/ITO—due to the band bending at the surface and a limited number of surface states that can act as electron transfer channels to overcome the energy barrier.

The fluorescence voltammograms of quantum dot ensembles show a highly reproducible dependence on the applied potential. When submonolayer concentrations are studied, the effect of the oxidation or reduction of nanocrystals can be detected very precisely in the luminescence signal, as opposed to the electric current, which is strongly affected by impurity reactions and by changes in the surface states of the electrode. The current due to electron transfer between the electrode and the quantum dots is orders of magnitude smaller than these residual currents and therefore not suited to draw any conclusions since it cannot reliably be differentiated.

The drop in luminescence and excited state lifetime at highly negative potentials makes it possible to determine the location of the nanocrystal conduction band edges by the onset of Auger quenching. Interesting differences between the substrates became visible: on an ITO substrate, the quantum dots show an additional fluorescence component that is always quenched on a Ga:ZnO/ITO substrate. This component seems to have a different quenching mechanism that is activated at potentials within the quantum dot band gap close to the first conduction band state, i.e. before the strong quenching seen on all of the studied substrates takes place. These observations hint at a complex interplay between the electrode's surface chemistry and the nanocrystals, and should be the subject of further studies.

An investigation of the impact of different reversal potentials hinted at the existence of short- and long-lived dark states that can be activated at specific potentials and show deactivation behavior that takes place in different potential regions and on different time scales.

First efforts were taken to investigate single nanocrystal fluorescence using a wide-field microscopy approach. This allows the observation of multiple quantum dots in parallel and therefore easily generates enough data to reproduce the ensemble voltammograms from single nanocrystal time traces and gives detailed information about their composition. It was found that the potential position for the onset of electron injection into the nanocrystal conduction band takes specific values different for each quantum dot. The size dispersion is not a decisive factor for the width of the injection edge distribution seen in the ensemble and single crystal observations. A change in the blinking dynamics is a likely cause for the broader distribution.

The method presented here allows several more applications, all of which have briefly been tested as a proof of concept. For example, single nanocrystals can be observed using confocal microscopy. This opens a pathway for a detailed blinking and lifetime analysis under specific electric potentials or oxidation states on the single quantum dot level.

Another interesting application are potential-resolved fluorescence spectra of the nanocrystal ensemble or even of single crystals. Quantum dots naturally show spectral diffusion, even without the influence of an electric potential or intentional charging. [46] This approach has not yet produced meaningful results, but may potentially make blue shifts due to oxidations at the core–shell interface visible, [99] or Stark effects from strong, local electric fields. [100]

Of course, the method is not limited to cyclic voltammetry. Applications such as potential-step voltammetry are promising candidates for a further investigation of the quenching and luminescence enhancement processes and for an analysis of time-resolved quenching or recovery dynamics.

Optically detected electrochemistry is a powerful tool for the study of electrode-adsorbed fluorophores in different oxidation states. The application to CdSe/ZnS nanocrystals that was established in this work provides a means to successfully control quantum dot fluorescence. The reproducible luminescence and lifetime responses in specific potential regions give hints towards the underlying processes. It became clear that there are several phenomena that defy any simple explanation, but are more likely the result of an interplay of different, more complex factors. The method makes a broad field of further investigation accessible.

Bibliography

[1] Xiaogang Peng, Michael C. Schlamp, Andreas V. Kadavanich, and A. P. Alivisatos. Epitaxial Growth of Highly Luminescent CdSe/CdS Core/Shell Nanocrystals with Photostability and Electronic Accessibility. *Journal of the American Chemical Society*, 119(30):7019–7029, July 1997. doi:10.1021/ja970754m.

[2] C. B. Murray, D. J. Norris, and M. G. Bawendi. Synthesis and characterization of nearly monodisperse CdE (E = sulfur, selenium, tellurium) semiconductor nanocrystallites. *Journal of the American Chemical Society*, 115(19):8706–8715, September 1993. doi:10.1021/ja00072a025.

[3] A. I. Ekimov, Al. L. Efros, and A. A. Onushchenko. Quantum size effect in semiconductor microcrystals. *Solid State Communications*, 56(11):921–924, December 1985. doi:10.1016/S0038-1098(85)80025-9.

[4] F. Hakimi, M. G. Bawendi, R. Tumminelli, and J. R. Haavisto. Quantum Dot Laser, November 9, 1993. US Patent 5,260,957 A.

[5] Marius Grundmann. The present status of quantum dot lasers. *Physica E: Low-dimensional Systems and Nanostructures*, 5(3):167–184, December 1999. doi:10.1016/S1386-9477(99)00041-7.

[6] Dmitri V. Talapin and Jonathan Steckel. Quantum dot light-emitting devices. *MRS Bulletin*, 38(09):685–691, September 2013. doi:10.1557/mrs.2013.204.

[7] V. L. Colvin, M. C. Schlamp, and A. P. Alivisatos. Light-emitting diodes made from cadmium selenide nanocrystals and a semiconducting polymer. *Nature*, 370(6488):354–357, August 1994. doi:10.1038/370354a0.

[8] A. J. Nozik. Quantum dot solar cells. *Physica E: Low-dimensional Systems and Nanostructures*, 14(1-2):115–120, April 2002. doi:10.1016/S1386-9477(02)00374-0.

[9] Lioz Etgar. Semiconductor Nanocrystals as Light Harvesters in Solar Cells. *Materials*, 6(2):445–459, February 2013. doi:10.3390/ma6020445.

[10] Igor L. Medintz, H. Tetsuo Uyeda, Ellen R. Goldman, and Hedi Mattoussi. Quantum dot bioconjugates for imaging, labelling and sensing. *Nature materials*, 4(6):435–46, June 2005. doi:10.1038/nmat1390.

[11] A. P. Alivisatos, Weiwei Gu, and Carolyn Larabell. Quantum Dots as Cellular Probes. *Annual Review of Biomedical Engineering*, 7:55–76, January 2005. doi:10.1146/annurev.bioeng.7.060804.100432.

[12] Charles Santori, Matthew Pelton, Glenn Solomon, Yseulte Dale, and Yoshihisa

Yamamoto. Triggered Single Photons from a Quantum Dot. *Physical Review Letters*, 86(8):1502–1505, February 2001. doi:10.1103/PhysRevLett.86.1502.

[13] R. Stevenson, R. Thompson, A. Shields, I. Farrer, B. Kardynal, D. Ritchie, and M. Pepper. Quantum dots as a photon source for passive quantum key encoding. *Physical Review B*, 66(8):081302, August 2002. doi:10.1103/PhysRevB.66.081302.

[14] M. Nirmal, B. O. Dabbousi, M. G. Bawendi, J. J. Macklin, J. K. Trautman, T. D. Harris, and L. E. Brus. Fluorescence intermittency in single cadmium selenide nanocrystals. *Nature*, 383(6603):802–804, October 1996. doi:10.1038/383802a0.

[15] Frank Cichos, Christian von Borczyskowski, and M. Orrit. Power-law intermittency of single emitters. *Current Opinion in Colloid & Interface Science*, 12(6):272–284, December 2007. doi:10.1016/j.cocis.2007.07.012.

[16] Kai Zhang, Hauyee Chang, Aihua Fu, A. Paul Alivisatos, and Haw Yang. Continuous distribution of emission states from single CdSe/ZnS quantum dots. *Nano letters*, 6(4):843–7, April 2006. doi:10.1021/nl060483q.

[17] Wei Qin and Philippe Guyot-Sionnest. Evidence for the Role of Holes in Blinking: Negative and Oxidized CdSe/CdS Dots. *ACS Nano*, 6(10):9125–9132, October 2012. doi:10.1021/nn303396c.

[18] Christophe Galland, Yagnaseni Ghosh, Andrea Steinbrück, Milan Sykora, Jennifer A. Hollingsworth, Victor I. Klimov, and Han Htoon. Two types of luminescence blinking revealed by spectroelectrochemistry of single quantum dots. *Nature*, 479(7372):203–207, November 2011. doi:10.1038/nature10569.

[19] Abey Issac, Cornelius Krasselt, Frank Cichos, and Christian von Borczyskowski. Influence of the dielectric environment on the photoluminescence intermittency of CdSe quantum dots. *ChemPhysChem*, 13(13):3223–30, September 2012. doi:10.1002/cphc.201101040.

[20] Marius Grundmann. Important crystal structures. In *The Physics of Semiconductors*, page 50. Springer, 2nd edition, 2010. ISBN 978-3-642-13883-6.

[21] Yong-Nian Xu and W. Ching. Electronic, optical, and structural properties of some wurtzite crystals. *Physical Review B*, 48(7):4335–4351, August 1993. doi:10.1103/PhysRevB.48.4335.

[22] Felix Bloch. Über die Quantenmechanik der Elektronen in Kristallgittern. *Zeitschrift für Physik*, 52(7-8):555–600, July 1929. doi:10.1007/BF01339455.

[23] David J. Norris. Electronic structure in semiconductor nanocrystals. In Victor I. Klimov, editor, *Nanocrystal Quantum Dots*, pages 63–96. CRC Press, Taylor and Francis Group, 2nd edition, 2010. ISBN 978-1-4200-7927-2.

[24] Sadao Adachi. Crystal structure. In *Properties of Group-IV, III-V and II-VI Semiconductors*, pages 4–6. John Wiley & Sons, Ltd., 2005. ISBN 0-470-09032-4.

[25] Moungi G. Bawendi, M. L. Steigerwald, and L. E. Brus. The Quantum Mechanics of Larger Semiconductor Clusters ("Quantum Dots").

Annual Review of Physical Chemistry, 41(1):477–496, October 1990. doi:10.1146/annurev.pc.41.100190.002401.

[26] Marius Grundmann. Mixed bonds. In *The Physics of Semiconductors*, pages 27–29. Springer, 2nd edition, 2010. ISBN 978-3-642-13883-6.

[27] A. P. Alivisatos. Perspectives on the Physical Chemistry of Semiconductor Nanocrystals. *The Journal of Physical Chemistry*, 100(31):13226–13239, January 1996. doi:10.1021/jp9535506.

[28] David J. Norris and Moungi. G. Bawendi. Measurement and assignment of the size-dependent optical spectrum in CdSe quantum dots. *Physical Review B*, 53 (24):16338–16346, June 1996. doi:10.1103/PhysRevB.53.16338.

[29] A. Baldereschi and Nunzio Lipari. Energy Levels of Direct Excitons in Semiconductors with Degenerate Bands. *Physical Review B*, 3(2):439–451, January 1971. doi:10.1103/PhysRevB.3.439.

[30] Peter Yu and Manuel Cardona. The $\vec{k} \cdot \vec{p}$ method of band-structure calculations. In *Fundamentals of Semiconductors: Physics and Materials Properties*, pages 68–82. Springer, 4th edition, 2010. ISBN 978-3-642-00710-1.

[31] Marius Grundmann. Band structure: Holes. In *The Physics of Semiconductors*, pages 169–170. Springer, 2nd edition, 2010. ISBN 978-3-642-13883-6.

[32] Holger T. Grahn. Density of states and carrier statistics. In *Introduction to Semiconductor Physics*, page 65. World Scientific, May 1999. ISBN 978-9-810-23302-0.

[33] Neil W. Ashcroft and N. David Mermin. Number of carriers in thermal equilibrium, chapter 28: Homogeneous semiconductors. In *Solid State Physics*, pages 572–575. Thomson Learning, Inc., 1976. ISBN 003-083993-9.

[34] V. A. Coleman and C. Jagadish. Basic properties and applications of ZnO. In Chennupati Jagadish and Stephen J. Pearton, editors, *Zinc Oxide Bulk, Thin Films and Nanostructures: Processing, Properties, and Applications*, page 7. Elsevier, 2011. ISBN 978-0-080-46403-9.

[35] Cadmium compounds (section 4.1.3.5). In Werner Martienssen and Hans Warlimont, editors, *Springer Handbook of Condensed Matter and Materials Data*, page 683. Springer, 2005. ISBN 3-540-44376-2.

[36] Al. L. Efros and A. L. Efros. Interband Absorption of Light in a Semiconductor Sphere. *Soviet Physics: Semiconductors*, 16:772, 1982.

[37] A. I. Ekimov, F. Hache, M. C. Schanne-Klein, D. Ricard, C. Flytzanis, I. A. Kudryavtsev, T. V. Yazeva, A. V. Rodina, and Al. L. Efros. Absorption and intensity-dependent photoluminescence measurements on CdSe quantum dots: assignment of the first electronic transitions. *Journal of the Optical Society of America B*, 10(1):100, January 1993. doi:10.1364/JOSAB.10.000100.

[38] D. J. Norris, A. Sacra, C. Murray, and M. G. Bawendi. Measurement of the size dependent hole spectrum in CdSe quantum dots. *Physical Review Letters*, 72(16): 2612–2615, April 1994. doi:10.1103/PhysRevLett.72.2612.

[39] Mark Schmidt, Sean Blanton, Margaret Hines, and Philippe Guyot-Sionnest. Size-dependent two-photon excitation spectroscopy of CdSe nanocrystals. *Physical Review B*, 53(19):12629–12632, May 1996. doi:10.1103/PhysRevB.53.12629.

[40] J. M. Ferreyra and C. R. Proetto. Quantum size effects on excitonic Coulomb and exchange energies in finite-barrier semiconductor quantum dots. *Physical Review B*, 60(15):10672–10675, October 1999. doi:10.1103/PhysRevB.60.10672.

[41] Ryan Cooney, Samuel Sewall, Kevin Anderson, Eva Dias, and Patanjali Kambhampati. Breaking the Phonon Bottleneck for Holes in Semiconductor Quantum Dots. *Physical Review Letters*, 98(17):177403, April 2007. doi:10.1103/PhysRevLett.98.177403.

[42] Philippe Guyot-Sionnest, Brian Wehrenberg, and Dong Yu. Intraband relaxation in CdSe nanocrystals and the strong influence of the surface ligands. *The Journal of Chemical Physics*, 123(7):074709, August 2005. doi:10.1063/1.2004818.

[43] Anjana Bagga, P. Chattopadhyay, and Subhasis Ghosh. Origin of Stokes shift in InAs and CdSe quantum dots: Exchange splitting of excitonic states. *Physical Review B*, 74(3):035341, July 2006. doi:10.1103/PhysRevB.74.035341.

[44] M. Nirmal, D. J. Norris, M. Kuno, M. G. Bawendi, Al. L. Efros, and M. Rosen. Observation of the "Dark Exciton" in CdSe Quantum Dots. *Physical Review Letters*, 75(20):3728–3731, November 1995. doi:10.1103/PhysRevLett.75.3728.

[45] Al. L. Efros, M. Rosen, M. Kuno, M. Nirmal, D. J. Norris, and M. G. Bawendi. Band-edge exciton in quantum dots of semiconductors with a degenerate valence band: Dark and bright exciton states. *Physical Review B*, 54(7):4843–4856, August 1996. doi:10.1103/PhysRevB.54.4843.

[46] S. A. Empedocles and M. G. Bawendi. Influence of Spectral Diffusion on the Line Shapes of Single CdSe Nanocrystallite Quantum Dots. *The Journal of Physical Chemistry B*, 103(11):1826–1830, March 1999. doi:10.1021/jp983305x.

[47] M. Kuno, D. P. Fromm, H. F. Hamann, A. Gallagher, and D. J. Nesbitt. Nonexponential "blinking" kinetics of single CdSe quantum dots: A universal power law behavior. *The Journal of Chemical Physics*, 112(7):3117, 2000. doi:10.1063/1.480896.

[48] K. Shimizu, R. Neuhauser, C. Leatherdale, S. Empedocles, W. Woo, and M. Bawendi. Blinking statistics in single semiconductor nanocrystal quantum dots. *Physical Review B*, 63(20):1–5, May 2001. doi:10.1103/PhysRevB.63.205316.

[49] H. Benisty, C. Sotomayor-Torrès, and C. Weisbuch. Intrinsic mechanism for the poor luminescence properties of quantum-box systems. *Physical Review B*, 44 (19):10945–10948, November 1991. doi:10.1103/PhysRevB.44.10945.

[50] Arthur J. Nozik. Spectroscopy and hot electron relaxation dynamics in semiconductor quantum wells and quantum dots. *Annual review of physical chemistry*, 52:193–231, January 2001. doi:10.1146/annurev.physchem.52.1.193.

[51] Philippe Guyot-Sionnest, Moonsub Shim, Chris Matranga, and Margaret Hines.

Intraband relaxation in CdSe quantum dots. *Physical Review B*, 60(4):R2181–R2184, July 1999. doi:10.1103/PhysRevB.60.R2181.

[52] Victor I. Klimov. Optical Nonlinearities and Ultrafast Carrier Dynamics in Semiconductor Nanocrystals. *The Journal of Physical Chemistry B*, 104(26):6112–6123, July 2000. doi:10.1021/jp9944132.

[53] Patanjali Kambhampati. Hot Exciton Relaxation Dynamics in Semiconductor Quantum Dots: Radiationless Transitions on the Nanoscale. *The Journal of Physical Chemistry C*, 115(45):22089–22109, November 2011. doi:10.1021/jp2058673.

[54] Al. L. Efros, V. A. Kharchenko, and M. Rosen. Breaking the phonon bottleneck in nanometer quantum dots: Role of Auger-like processes. *Solid State Communications*, 93(4):281–284, January 1995. doi:10.1016/0038-1098(94)00760-8.

[55] J. C. Rivière. Auger electron spectroscopy. *Contemporary Physics*, 14(6):513–539, November 1973. doi:10.1080/00107517308210772.

[56] V. A. Kharchenko and M. Rosen. Auger relaxation processes in semiconductor nanocrystals and quantum wells. *Journal of Luminescence*, 70(1-6):158–169, October 1996. doi:10.1016/0022-2313(96)00052-X.

[57] Marcus Jones, Shun S. Lo, and Gregory D. Scholes. Quantitative modeling of the role of surface traps in CdSe/CdS/ZnS nanocrystal photoluminescence decay dynamics. *Proceedings of the National Academy of Sciences of the United States of America*, 106(9):3011–6, March 2009. doi:10.1073/pnas.0809316106.

[58] S. Roy Morrison. Comparison of the Various Surface States and Sites (4.2.4). In *The Chemical Physics of Surfaces*, page 121. Springer, Boston, MA, 1st edition, 1977. ISBN 978-1-4615-8009-6. doi:10.1007/978-1-4615-8007-2.

[59] Jacek Jasieniak and Paul Mulvaney. From Cd-rich to Se-rich – the Manipulation of CdSe Nanocrystal Surface Stoichiometry. *Journal of the American Chemical Society*, 129(10):2841–8, March 2007. doi:10.1021/ja066205a.

[60] Joseph R. Lakowicz. Intensity Decay Laws. In *Principles of Fluorescence Spectroscopy*, chapter 4.11., pages 141–143. 3rd edition, 2006.

[61] Rüdiger Memming. *Semiconductor Electrochemistry*. Wiley-VCH, 1st edition, 2001. ISBN 3-527-30147-X.

[62] Ü. Özgür, Ya. I. Alivov, C. Liu, A. Teke, M. A. Reshchikov, S. Doğan, V. Avrutin, S.-J. Cho, and H. Morkoç. A comprehensive review of ZnO materials and devices. *Journal of Applied Physics*, 98(4):041301, 2005. doi:10.1063/1.1992666.

[63] H. Kim, C. M. Gilmore, A. Piqué, J. S. Horwitz, H. Mattoussi, H. Murata, Z. H. Kafafi, and D. B. Chrisey. Electrical, optical, and structural properties of indium–tin–oxide thin films for organic light-emitting devices. *Journal of Applied Physics*, 86(11):6451, 1999. doi:10.1063/1.371708.

[64] Krishnan Rajeshwar. Fundamentals of Semiconductor Electrochemistry and Photoelectrochemistry. In Allen J. Bard, editor, *Encyclopedia of Electrochem-*

istry. Wiley-VCH, Weinheim, Germany, December 2007. ISBN 3527610421. doi:10.1002/9783527610426.

[65] W. B. Russel, D. A. Saville, and W. R. Schowalter. *Colloidal Dispersions*. Cambridge University Press, Cambridge, 1989. ISBN 9780511608810. doi:10.1017/CBO9780511608810.

[66] Allen J. Bard and Larry R. Faulkner. Semiempirical Treatment of Nernstian Reactions with Coupled Chemical Reactions. In *Electrochemical Methods: Fundamentals and Applications*, page 36. Wiley, 2nd edition, 2001. ISBN 978-0-471-04372-0.

[67] Evident Technologies. EviDots Specification. Technical Report October, 2006.

[68] Markus Grabolle, Jan Ziegler, Alexei Merkulov, Thomas Nann, and Ute Resch-Genger. Stability and Fluorescence Quantum Yield of CdSe-ZnS Quantum Dots–Influence of the Thickness of the ZnS Shell. *Annals of the New York Academy of Sciences*, 1130:235–41, January 2008. doi:10.1196/annals.1430.021.

[69] B. O. Dabbousi, J. Rodriguez-Viejo, F. V. Mikulec, J. R. Heine, H. Mattoussi, R. Ober, K. F. Jensen, and M. G. Bawendi. (CdSe)ZnS Core–Shell Quantum Dots: Synthesis and Characterization of a Size Series of Highly Luminescent Nanocrystallites. *The Journal of Physical Chemistry B*, 101(46):9463–9475, November 1997. doi:10.1021/jp971091y.

[70] D. Gidalevitz, Z. Huang, and S. A. Rice. Urease and Hexadecylamine-Urease Films at the Air-Water Interface: An X-Ray Reflection and Grazing Incidence X-Ray Diffraction Study. *Biophysical journal*, 76(5):2797–802, May 1999. doi:10.1016/S0006-3495(99)77433-3.

[71] C. Bullen and P. Mulvaney. The effects of chemisorption on the luminescence of CdSe quantum dots. *Langmuir*, 22(7):3007–13, March 2006. doi:10.1021/la051898e.

[72] Robert H. Webb. Confocal optical microscopy. *Reports on Progress in Physics*, 59(3):427–471, March 1996. doi:10.1088/0034-4885/59/3/003.

[73] Aron Walsh, Juarez Da Silva, Su-Huai Wei, C. Körber, A. Klein, L. Piper, Alex DeMasi, Kevin E. Smith, G. Panaccione, P. Torelli, D. Payne, A. Bourlange, and R. Egdell. Nature of the Band Gap of In_2O_3 Revealed by First-Principles Calculations and X-Ray Spectroscopy. *Physical Review Letters*, 100(16):167402, April 2008. doi:10.1103/PhysRevLett.100.167402.

[74] Michael Lorenz, Holger Hochmuth, Christoph Grüner, Helena Hilmer, Alexander Lajn, Daniel Spemann, Matthias Brandt, Jan Zippel, Rüdiger Schmidt-Grund, Holger von Wenckstern, and Marius Grundmann. Oxide Thin Film Heterostructures on Large Area, with Flexible Doping, Low Dislocation Density, and Abrupt Interfaces: Grown by Pulsed Laser Deposition. *Hindawi Publishing: Laser Chemistry*, 2011. doi:10.1155/2011/140976.

[75] Shengye Jin, Nianhui Song, and Tianquan Lian. Suppressed blinking dy-

namics of single QDs on ITO. *ACS Nano*, 4(3):1545–52, March 2010. doi:10.1021/nn901808f.

[76] Praket P. Jha and Philippe Guyot-Sionnest. Electrochemical Switching of the Photoluminescence of Single Quantum Dots. *The Journal of Physical Chemistry C*, 114(49):21138–21141, December 2010. doi:10.1021/jp1074626.

[77] Yeon Sik Jung. Spectroscopic ellipsometry studies on the optical constants of indium tin oxide films deposited under various sputtering conditions. *Thin Solid Films*, 467(1-2):36–42, November 2004. doi:10.1016/j.tsf.2004.02.047.

[78] Dai Zhong-Hong, Zhang Rong-Jun, Shao Jie, Chen Yi-Ming, Zheng Yu-Xiang, Wu Jia-Da, and Chen Liang-Yao. Optical Properties of Zinc-oxide Films Determined UsingSpectroscopic Ellipsometry with Various Dispersion Models. *Journal of the Korean Physical Society*, 55(32):1227, September 2009. doi:10.3938/jkps.55.1227.

[79] G. Gritzner and J. Kuta. Recommendations on reporting electrode potentials in nonaqueous solvents. *Pure and Applied Chemistry*, 56(4):461–466, 1984. doi:10.1351/pac198456040461.

[80] Neil G. Connelly and William E. Geiger. Chemical Redox Agents for Organometallic Chemistry. *Chemical Reviews*, 96(2):877–910, January 1996. doi:10.1021/cr940053x.

[81] D. Tsiplakides and C. G. Vayenas. The Absolute Potential Scale in Solid State Electrochemistry. *Solid State Ionics*, 152-153:625–639, December 2002. doi:10.1016/S0167-2738(02)00396-X.

[82] Jeanne Diane Sinsheimer. *Electrochemistry of Ferrocene Compounds*. California State University, Long Beach, 1986.

[83] S. Trasatti. The Absolute Electrode Potential: An Explanatory Note (Recommendations 1986). *Pure and Applied Chemistry*, 58(7), January 1986. doi:10.1351/pac198658070955.

[84] Mansoor Namazian, Ching Yeh Lin, and Michelle L. Coote. Benchmark Calculations of Absolute Reduction Potential of Ferricinium/Ferrocene Couple in Nonaqueous Solutions. *Journal of Chemical Theory and Computation*, 6:2721–2725, 2010. doi:10.1021/ct1003252.

[85] S. N. Frank and Allen J. Bard. Semiconductor Electrodes. II. Electrochemistry at n-Type Titanium Dioxide Electrodes in Acetonitrile Solutions. *Journal of the American Chemical Society*, 97(26):7427–7433, December 1975. doi:10.1021/ja00859a007.

[86] Nicola A. Hill and K. Birgitta Whaley. A theoretical study of the influence of the surface on the electronic structure of CdSe nanoclusters. *The Journal of Chemical Physics*, 100(4):2831, 1994. doi:10.1063/1.466477.

[87] J. E. Bowen Katari, V. L. Colvin, and A. P. Alivisatos. X-Ray Photoelectron Spectroscopy of CdSe Nanocrystals with Applications to Studies of the Nanocrys-

tal Surface. *The Journal of Physical Chemistry*, 98(15):4109–4117, April 1994. doi:10.1021/j100066a034.

[88] Rüdiger Memming. Solid-Liquid Interface. In *Semiconductor Electrochemistry*, chapter 5, page 81. Wiley-VCH, 1st edition, 2001. ISBN 3-527-30147-X.

[89] V. Christou, M. Etchells, O. Renault, P. J. Dobson, O. V. Salata, G. Beamson, and R. G. Egdell. High resolution x-ray photoemission study of plasma oxidation of indium–tin–oxide thin film surfaces. *Journal of Applied Physics*, 88(9):5180, 2000. doi:10.1063/1.1312847.

[90] Fang-Ling Kuo, Yun Li, Marvin Solomon, Jincheng Du, and Nigel D. Shepherd. Workfunction tuning of zinc oxide films by argon sputtering and oxygen plasma: an experimental and computational study. *Journal of Physics D: Applied Physics*, 45(6):065301, February 2012. doi:10.1088/0022-3727/45/6/065301.

[91] Tiffany C. Kaspar and Tim C. Droubay. Variation in band offsets at ZnO/Sn:In2O3 heterojunctions measured by x-ray photoelectron spectroscopy. *Journal of Vacuum Science & Technology A: Vacuum, Surfaces, and Films*, 30(4): 04D112, 2012. doi:10.1116/1.4719541.

[92] Bang-Tai Tang, Qing-Xuan Yu, Hsin-Ying Lee, and Ching-Ting Lee. Ohmic performance of ZnO and ITO/ZnO contacted with n-type GaN layer. *Materials Science and Engineering: B*, 82(1-3):259–261, May 2001. doi:10.1016/S0921-5107(00)00760-1.

[93] Sang-Ho Kim, Dea-Kue Hwang, Seong-Ju Park, and Tae-Yeon Seong. Carrier Concentration Dependence of the Electrical Behaviors of ITO Contacts on n-Type ZnO. *Journal of the Korean Physical Society*, 54(2):740, February 2009. doi:10.3938/jkps.54.740.

[94] Jacek Jasieniak, Marco Califano, and Scott E. Watkins. Size-Dependent Valence and Conduction Band-Edge Energies of Semiconductor Nanocrystals. *ACS Nano*, 5(7):5888–902, July 2011. doi:10.1021/nn201681s.

[95] Su-Huai Wei and Alex Zunger. Calculated natural band offsets of all II–VI and III–V semiconductors: Chemical trends and the role of cation d orbitals. *Applied Physics Letters*, 72(16):2011, 1998. doi:10.1063/1.121249.

[96] Wei Qin, Raman A. Shah, and Philippe Guyot-Sionnest. CdSeS/ZnS alloyed nanocrystal lifetime and blinking studies under electrochemical control. *ACS Nano*, 6(1):912–8, January 2012. doi:10.1021/nn2044388.

[97] Pravin P. Ingole, Stephen G. Hickey, Christian Waurisch, Nikolai Gaponik, and Alexander Eychmüller. Effect of Electrochemical Charge Injection on the Photoluminescence Properties of CdSe Quantum Dot Monolayers Anchored to Oxide Substrates. *Zeitschrift für Physikalische Chemie*, 227:130311033635007, March 2013. doi:10.1524/zpch.2013.0371.

[98] V. I. Klimov, A. A. Mikhailovsky, D. W. McBranch, C. A. Leatherdale, and M. G. Bawendi. Quantization of Multiparticle Auger Rates in Semi-

conductor Quantum Dots. *Science*, 287(5455):1011–1013, February 2000. doi:10.1126/science.287.5455.1011.

[99] Wilfried G. J. H. M. van Sark, Patrick L. T. M. Frederix, Ageeth A. Bol, Hans C. Gerritsen, and Andries Meijerink. Blueing, Bleaching, and Blinking of Single CdSe/ZnS Quantum Dots. *ChemPhysChem*, 3(10):871–879, October 2002. doi:10.1002/1439-7641(20021018)3:10<871::AID-CPHC871>3.0.CO;2-T.

[100] S. A. Empedocles and M. G. Bawendi. Quantum-Confined Stark Effect in Single CdSe Nanocrystallite Quantum Dots. *Science*, 278(5346):2114–2117, December 1997. doi:10.1126/science.278.5346.2114.

Acknowledgements

Many people helped in the making of this work and they deserve a big »Thank you!« for their efforts.

Prof. Dr. Frank Cichos supervised this Master thesis and helped with fresh ideas and by sharing his experiences. He is never short on encouragements and advice, and also never short on Brötchen for the department breakfast.

Dr. Johannes Schwarz from the Kurt-Schwabe-Institut in Meinsberg helped with advice in the field of electrochemistry, did valuable reference measurements and loaned a commercial potentiostat to verify the correct function of the home-made model used for this work.

Prof. Dr. Bernd Abel took the time to review this thesis. In the early stages of this work, his Physical Chemistry group gave unconditional support by providing access to both a fluorescence and an absorption spectrometer. Dr. Ralf Hermann and Dr. Tilmann Häupl were particularly helpful with introducing me to the devices.

Dipl. Phys. Uwe Weber is the department's guy to go when it comes to applying science to the real world. He built the home-made potentiostat that was used in this work and has plenty of tools at hand whenever there is the need for technical help.

My family was always supportive throughout my whole studies and in particular, my dad helped me to understand the electric circuitry of the potentiostat and to resolve issues with the device.

All members of the Molecular Nanophotonics group never shy to discuss new challenges and actively take part in resolving problems. Advice is shared, and the open environment is certainly invaluable for scientific work.

A huge »Thank you!« goes to Dipl. Phys. Nicole Amecke. She is always very helpful and friendly when support is needed, introduced me to the quantum dots, let me work with her microscope setup, showed a lot of trust and never hesitated to give advice and share her experience.

Thank you all!

Selbstständigkeitserklärung

Hiermit erkläre ich, dass ich die vorliegende Masterarbeit selbständig verfasst habe und keine anderen als die angegebenen Quellen und Hilfsmittel benutzt habe. Alle Stellen der Arbeit, die wörtlich oder sinngemäß aus Veröffentlichungen oder aus anderweitigen fremden Äußerungen entnommen wurden, sind als solche kenntlich gemacht. Ferner erkläre ich, dass die Arbeit noch nicht in einem anderen Studiengang als Prüfungsleistung verwendet wurde.

<div align="right">

David Plotzki

Leipzig, 03. November 2014

</div>

Ich bin einverstanden, dass die Arbeit nach positiver Begutachtung in der Universitätsbibliothek zur Verfügung steht.

<div align="right">

David Plotzki

Leipzig, 03. November 2014

</div>